Biointerface Research in Applied Chemistry
Open-Access Journal (ISSN: 2069-5837)

Article
Volume 16, Issue 2, 2026, 64
https://doi.org/10.33263/BRIAC162.064

Integrated Enzyme and Computational Screening of Plant-Derived Phytoconstituents as Alpha-Amylase Inhibitors

Bishnu P. Marasini [1,2], Pratima Gautam [1], Prabhat Neupane [3], Manila Poudel [1], Sujan Dhital [3], Binita Maharjan [3], Timila Shrestha [3], Samjhana Bharati [3], Trishna Manandhar [1], Jhashanath Adhikari Subin [4,*], Ram Lal Swagat Shrestha [3,*]

[1] Nepal Health Research Council, Ministry of Health and Population, Ramshah Path, Kathmandu 44600, Nepal; bishnu.marasini@gmail.com;
[2] Department of Chemistry, Amrit Campus, Tribhuvan University, Lainchaur, Kathmandu 44600, Nepal; neupaneprabhat1998@gmail.com (P.N.); sujandhital07@gmail.com (S.D.); binitamhrjan@gmail.com (B.M.); timilastha@gmail.com (T.S.); bharati.samjhana@gmail.com (S.B.); swagatstha@gmail.com (R.L.S.S.);
[3] Bioinformatics and Cheminformatics Division, Scientific Research and Training Nepal P. Ltd., Bhaktapur 44800, Nepal; subinadhikari2018@gmail.com;
[4] Department of Biotechnology, National College, Tribhuvan University, Lainchour, Kathmandu 44600, Nepal; bishnu.marasini@gmail.com (B.P.M.); gautam.pratima11@gmail.com (P.G.); paudelmanila@gmail.com (M.P.); trishna_mdr@hotmail.com (T.M.);
* Correspondence: subinadhikari2018@gmail.com (J.A.S.); swagatstha@gmail.com (R.L.S.S.);

Received: 3.01.2025; Accepted: 27.07.2025; Published: 15.04.2026

Abstract: Alpha-amylase plays a key role in carbohydrate metabolism and is a validated target for managing type 2 diabetes. This study aimed to identify natural α-amylase inhibitors from 16 ethnobotanically important plants. Methanolic extracts were screened for antioxidant and enzyme inhibition activity. Seven extracts showed notable α-amylase inhibition, with inhibitory concentration (IC_{50}) values ranging from 44.7±2 to 313.1±4 µg/mL and antioxidant activity between 17.0% and 40.81%. A total of 122 phytochemicals from the active extracts were subjected to molecular docking against α-amylase (PDB ID: 4GQR), revealing strong binding affinities (-9.4 to -8.0 kcal/mol) for key compounds such as lawnermis acid and apigenin-7-O-rutinoside. The top candidates were further evaluated through 200 ns molecular dynamics simulations. Stability was confirmed by root-mean-square deviation, solvent accessible surface area, radius of gyration, and hydrogen bond analysis, while MMPBSA-based binding free energy calculations supported spontaneous and thermodynamically stable interactions. These findings suggest that the selected phytoconstituents hold promise as natural inhibitors of α-amylase and warrant further *in vitro*, *in vivo*, and pharmacokinetic studies for potential development into anti-diabetic therapeutics.

Keywords: alpha-amylase; binding free energy; type 2 diabetes mellitus; molecular docking; molecular dynamics simulation; natural inhibitors.

1. Introduction

Diabetes mellitus (DM) is a disease characterized by insufficient glucose control in the blood. The main subtypes of DM are Type 1 (T1DM) with reduced insulin secretion and Type 2 (T2DM) with reduced insulin effectiveness. T1DM occurs in youth, while T2DM is linked

to unhealthy lifestyles in older adults [1]. It is a complicated disorder characterized by abnormalities in glucose, protein, and lipid metabolism [2]. According to estimates from the International Diabetes Federation, the prevalence of diabetes, which was 10.5% in 2021, is expected to increase to 11.3% by 2030 and further to 12.2% by 2040 [3, 4].

Alpha-amylase (α-amylase), also recognized as α-1, 4 glucan-4-glucanohydrolase (EC 3.2.1.1), is an enzyme predominantly located in the pancreas and secreted by salivary glands. Its primary role is to catalyze the hydrolysis of complex carbohydrates, such as starch and glycogen, into simpler sugars. Inhibition of α-amylase disrupts starch breakdown in the intestine, slowing digestion and providing an effective approach for the management of hyperglycemic conditions [5]. Acarbose and miglitol, two inhibitors currently used in clinical settings, act by inhibiting α-amylase [6]. However, many synthetic hypoglycemic drugs face inherent limitations, lack specificity, trigger severe adverse reactions, and prove insufficient in addressing the complications associated with diabetes. The principal side effects of these inhibitors occur in the digestive system, leading to symptoms such as bloating, abdominal discomfort, diarrhea, and flatulence [7]. In contrast, herbal remedies are increasingly favored for diabetes treatment due to their lack of adverse effects and cost-effectiveness compared with synthetic hypoglycemic medications [8]. It is estimated that over 200 plant species demonstrate properties that can lower blood sugar levels [9, 10]. Plant-based phytoconstituents are capable of inhibiting α-amylase, making them a safer option for regulating blood glucose levels in T2DM [11-13]. Research indicates that the effectiveness of plant polyphenols is associated with their antioxidant activity, and many of these plants also exhibit properties that can lower blood sugar levels [14].

The field of in silico molecular docking is rapidly advancing, providing insights into and predicting potential modes of interaction between a ligand and a target biomolecule [15, 16]. The study's objective was to perform a docking analysis on the principal components extracted from selected methanolic plant extracts. The overarching aim is to investigate the therapeutic potential of the identified plant extracts for combating diabetes, employing a dual approach that combines experimental evidence with molecular docking and molecular dynamics simulations.

2. Materials and Methods

1.1. Chemicals and reagents.

Acarbose, Porcine pancreatic alpha-amylase (PPA), and 2-chloro-4-nitrophenyl-α-D-maltotrioside were acquired from Sigma-Aldrich, Germany. Gallic acid and 2, 2-diphenyl-1-picryl hydrazine were procured from Molychem and Hi-media, India. Quercetin, dimethyl sulphoxide (DMSO), sodium dihydrogen orthophosphate (NaH_2PO_4), disodium hydrogen orthophosphate (Na_2HPO_4), and various other necessary chemicals were obtained from Fischer-Scientific, India.

1.2. Collection and identification of plant samples.

Plant species were collected from various regions across Nepal in 2018 (Table 1). The selection of these plant samples was guided by a comprehensive synthesis of ethnobotanical wisdom from local custodians, principles of Ayurveda, references from the Herbarium center, and a thorough examination of relevant literature. The precise botanical nomenclature of the

collected plant samples was ascertained through formal identification procedures conducted at the National Herbarium and Research Center situated in Godawari, Nepal.

Table 1. List of plants collected for the study.

S.N.	Scientific names of plant samples	Local name	Plant parts used	Collection site
1.	*Hypericum uralum* Buch. -Ham	Yurilo	leaf with stem	Lalitpur
2.	*Myrica esculenta* Buch. -Ham	Kafal	Leaf	Bhaktapur
3.	*Chrysanthemum indicum*	Godawari	Whole plant	Lalitpur
4.	*Boerhavia spp.*	Punarnava	Leaf	Hetauda
5.	*Ageratina adenophora* Spreng.	Banmara	Leaf with stem	Kathmandu
6.	*Lawsonia inermis* Linn.	Henna	Leaf	Chitwan
7.	*Morus australis* Poir.	Kimbu	Leaf	Parbat
8.	*Cinnamomum glanduliflerum* Wall.	Kapur	Leaf	Chitwan
9.	*Eclipta prostrate* Linn.	Bhringaraja	Leaf	Kathmandu
10.	*Bunium bulbocastanum* Linn.	Kalojeera	Leaf with stem	Argakhanchi
11.	*Persea Americana* Mill.	Avocado	Leaf	Lalitpur
12.	*Urtica ardens* Link	Sisnoo	Whole plant	Baglung
13.	*Picorrhiza kurroa* Royle ex Benth.	Kutki	Leaf	Butwal
14.	*Psidium guajava* Linn.	Guava	Leaf	Chitwan
15.	*Piper cubeba* L. f.	Sitalchini	Leaf	Sauraha
16.	*Prunus persica* Linn.	Aaru	Leaf	Lalitpur

2.3. Preparation of methanolic extracts.

Initially, the methanolic extracts of various plant specimens were prepared using the cold-percolation method as outlined by Duraipandiyan *et al*. [17]. The filtrate was concentrated under vacuum using a rotary evaporator at a controlled temperature of 55°C.

The percentage yield of the methanolic extract was calculated by the following formula (1):

$$\% \text{ yield} = \frac{\text{Dry weight of extract}}{\text{Dry weight of plant material}} \times 100 \qquad (1)$$

2.4. Determination of total phenolic content.

For the total polyphenolic content of the plant extract, a colorimetric procedure, as described by Ainsworth and Gillespie [18] and Lu *et al*. [19] with slight modifications, was used. Initially, 20 µL of gallic acid (GA) at various concentrations was loaded onto a 96-well plate in triplicate, with the GA concentration increasing stepwise. Following this, 20 µL of a 50% DMSO solution was placed in triplicate in the four corners of the plate as a negative control. Subsequently, 20 µL of the 500 µg/mL plant extract was added to the remaining wells in triplicate. To each well, 110 µL of distilled water was introduced, followed by the addition of 100 µL of the FC reagent and 80 µL of the Na_2CO_3 solution, ensuring a final volume of 200 µL in each well. At room temperature, the plate was then incubated in the dark for 15 minutes, and the absorbance was measured at 765 nm using a microplate reader (Epoch 2, BioTek Instruments, Inc., USA). A standard curve was constructed using standard GA solutions ranging from 10 to 80 µg/mL. The extract's concentration of total phenolic compounds in the extracts was determined in milligrams of GA equivalent per gram of dry weight (mg GAE/g) based on the GA standard curve.

2.5. Determination of total flavonoid content.

The TFC assay was conducted on a 96-well plate using a colorimetric method with slight modifications based on the procedure outlined by Chang *et al*. [20]. Initially, quercetin (130 µL) at different concentrations was dispensed onto the 96-well plate, following a

progressive concentration order. DMSO served as a negative control as described in the previous method. Furthermore, 20 µL of the 500 µg/mL plant extract was added to the remaining wells in triplicate.

To each well containing the plant sample and the negative control, 110 µL of distilled water was added, followed by sequential additions of 60 µL of ethanol, 5 µL of $AlCl_3$, and 5 µL of potassium acetate, resulting in a final volume of 200 µL in each well. At room temperature, the plate was then incubated in the dark for 30 minutes, and the absorbance was subsequently measured at 415 nm using a microplate reader (Epoch 2, BioTek Instruments, Inc., USA). A standard curve was constructed using standard quercetin solutions ranging from 10 to 80 µg/mL. The concentration of total flavonoid compounds in the extracts was expressed as milligrams of quercetin equivalent per gram of dry weight (mg QE/g), determined from a quercetin standard curve.

2.6. Determination of antioxidant activity.

The assessment of antioxidant activity in various plant samples was conducted on a 96-well plate with a slight modification to the colorimetric method. In this evaluation, a positive control consisting of 20 µg/mL of quercetin and a negative control utilizing 50% DMSO were employed. For each test, 100 µL of the positive control, DMSO, and the plant extracts were individually loaded into the 96-well plate in triplicate. Additionally, 100 µL of a DPPH solution was introduced into each well, ensuring a final volume of 200 µL. The plate was then subjected to a 30-minute incubation period at room temperature in the dark. Subsequently, absorbance readings were obtained at 517 nm using a microplate reader (Epoch 2, BioTek Instruments, Inc., USA). The DPPH radical scavenging activity was determined by applying the following equation (2):

$$\% \text{ Inhibition} = \frac{\text{Ccontrol} - \text{Ssample}}{\text{Ccontrol}} * 100 \qquad (2)$$

Where C is the absorbance of control (DMSO), and S is the absorbance of the sample.

2.7. Alpha-amylase inhibition assay.

The assessment of alpha-amylase inhibition activity was carried out using a 50 mM phosphate buffer with a pH of 6.8. The entire experiment was conducted in a 96-well plate, wherein Acarbose served as the positive control, and DMSO functioned as the negative control. Initially, 80 µL of pancreatic alpha-amylase at a final concentration of 1.5 Units/mL was introduced into each well. Subsequently, 20 µL of test compounds, prepared in DMSO, were added, and the mixture was incubated at 37°C for 15 minutes. Following this, the initial absorbance was recorded. The enzymatic reaction was initiated by adding 100 µL of substrate CNPG3 (375 µM), which was prepared in the aforementioned buffer, thereby maintaining a final volume of 200 µL. The change in absorbance resulting from the release of p-nitroaniline was continuously monitored at 405 nm, following the methodology described by [21]. DMSO was used as the negative control, as it did not exhibit any inhibitory effect up to 5% on α-amylase inhibition. The IC_{50} value, representing the concentration at which 50% inhibition occurred, was determined using the EZ-fit enzyme kinetics program, provided by Perellela Scientific, Inc., Amherst, Mars, USA. The percentage α-amylase inhibitory effect was calculated by the following formula (3):

$$\% \text{ inhibition} = \frac{Ao - At}{Ao} \times 100 \qquad (3)$$

Where A_o is the absorbance of the enzyme-substrate reaction with 5% DMSO, and A_t is the absorbance of the enzyme-substrate reaction with plant extract.

2.8. Statistical analysis.

The outcomes of the spectrophotometric tests, such as those involving enzyme assays, were managed using the Gen5 Microplate software. Additionally, Microsoft Excel (2016) was utilized for supplementary data analysis. The IC_{50} (representing the inhibition of enzymatic substrate hydrolysis by 50%) was determined with the EZ-Fit software (Perellela Scientific, Inc., Amherst, Mars, USA). Results were reported as the mean value ± standard error from three separate experiments.

2.9. Computational study.

2.9.1. Selection and preparation of ligands.

A total of 122 reported compounds of seven plants (Chrysanthemum indicum [22-25], Lawsonia inermis [26-33], Hypericum uralum [34], Ageratina adenophora [35-41], Persea americana [42, 43], Myrica esculenta [44-49], and Cinnamomum glanduliferum) [50-54] were used as a database of ligands for computational evaluation of their therapeutic potential against diabetes (Figure S1). Firstly, the 2D structures of ligands were drawn in Cdx format and converted to 3D PDB format using the ChemDraw program [55]. Structural optimization of the prepared 3D molecules was performed using the Avogadro software [56]. Geometry optimization was conducted using the Universal Force Field (UFF) with the conjugate gradient algorithm for up to 2000 steps, ensuring energy convergence ($\Delta E = 0$). Additionally, energy minimization was carried out to refine molecular conformations, and bond orders were verified for each molecule to confirm structural integrity. Then, the PDB file of the ligands was converted to PDBQT format utilizing AutoDock Tools [57].

2.9.2. Target selection and preparation of structure.

The crystal structure of human pancreatic α-amylase (HPAA) (PDB ID: 4GQR) with an X-ray diffraction resolution of 1.20 Å was retrieved from the RCSB database [58]. Since the α-amylase protein contained no missing amino acid residues, homology modeling wasn't deemed necessary [59]. Using PyMOL, the protein was cleaned by removing water molecules, ions, and non-standard amino acid residues. Once the polar hydrogen atoms and Kollman charges were added, AutoDock Tools was used to convert the file to the pdbqt format.

2.9.3. Molecular docking calculations.

Molecular docking was carried out using AutoDock Vina software. The grid center of (16.731, 17.235, 42.467) and box size of 44×46×44 $Å^3$ with 0.375 Å spacing, and exhaustiveness of 32 were applied, covering the catalytic site of the protein. Through molecular docking calculations, energy minima were attained, and the best-docked ligand at the catalytic site of the α-amylase protein was identified based on its binding affinity (kcal/mol). The scoring function comprises several stabilizing (E_{Gauss1}, E_{Gauss2}, $E_{Hydrogen\ Bond}$, and $E_{Hydrophobic}$) and destabilizing components ($E_{Repulsion}$, $E_{Rotational}$) [57]. Validation of the molecular docking calculation was done through the superposition of the docked native ligand with the ligand in

the crystalline protein. An acceptable RMSD value of 2.5 Å was obtained [60-62]. Protein-ligand interactions were visualized in 2D and 3D representations using the Biovia Discovery Studio application. The pose with the optimal binding energies was chosen for analysis, additional investigation, and molecular dynamics simulation.

2.9.4. Molecular dynamics simulation.

The GROMACS program was used for molecular dynamics simulation (MDS) of best-docked ligands [63]. CHARMM27 force field [64] from the SwissParam server [65] was used for protein and the ligand, respectively. A triclinic box of 10 Å dimensions was solvated using the TIP3P water model. The system was neutralized by an isotonic solution of NaCl (0.15 M). Then, at an optimal temperature of 310 K and a pressure of 1 bar, the system was equilibrated in four stages: the first two NVT equilibria (600 ps and 500 ps) and the final two NPT equilibria (500 ps each). Temperature and pressure coupling were performed using a modified Berendsen thermostat and the isotropic Parrinello-Rahman method, respectively. Several parameters, including SASA, RMSD, R_g, and RMSF, were retrieved from the MDS trajectory during the final production run for 200 ns without any constraints using the built-in modules of the GROMACS program.

2.9.5. Binding free energy changes (MMPBSA method) estimation.

The Poisson-Boltzmann solvation model [66] was used to determine changes in binding free energy throughout complex formation and in the equilibrated portion (20 ns) of the trajectory. Based on changes in binding free energy, the spontaneity and feasibility of the forward reaction were assessed.

The changes in binding free energy of the protein-ligand complex are given by the linear equation (4) [67]:

$$\Delta G_{BFE} = \Delta G_{complex} - \Delta G_{protein} - \Delta G_{ligand} \quad (4)$$

$$\Delta G_{BFE} = \Delta G_{gas} + \Delta G_{solvent} \quad (5)$$

And, it can be decomposed as equation (6)

$$\Delta G_{BFE} = \Delta G_{VDW} + \Delta G_{EL} + \Delta G_{PB} + \Delta G_{SURF} \quad (6)$$

Equation (5)'s right-hand side has two components that represent gas phase energies (ΔG_{gas}) and solvation ($\Delta G_{solvent}$), respectively.

3. Results and Discussion

3.1. Total phenolic and flavonoid content in the extract.

The TPC ranged from (0.41±0.05 to 24.29±0.07) mg GAE/gm, with *P. guajava* displaying the highest phenolic content and *P. persica* demonstrating the lowest among all the methanolic extracts from various plants (Table S1). The calculated TFC of the chosen plant extracts fell within a range, spanning from 1.24 mg QE/gm to 18.16±0.05 mg QE/gm. Notably, *H. uralum* exhibited the highest TFC, while *P. persica* had the lowest TFC (Table S2). In our study, the TPC of *A. adenophora* was determined to be 6.04±0.01 mg GAE/g, which is lower than the TPC reported in a study by Tripathi and Saini for the methanolic extract of *A. adenophora* (30.71±0.16 mg GAE/g) [68]. Similarly, a study by Regmi and Sharma also

revealed a TPC value of 67.74 mg GAE/g [69]. The disparity in values could be attributed to differences in genetic backgrounds, environmental factors, cultural factors, and agronomic techniques [70, 71]. Our TPC result for *A. adenophora* is found to be similar to that of a study done by Kapali and Sharma [72], 4.70±0.122 mg QE/g. Additionally, *M. esculenta* exhibited favorable TPC and TFC values (24.25±0.03 mg GAE/g and 10.31±0.04 mg QE/g). In contrast, Kabra *et al*. (2019) reported higher levels for both TPC and TFC (88.94±0.24 mg GAE/g and 67.44±0.14 mg QE/g) [73]. These variations in content may be explained by the factors mentioned earlier. The increased phenolic content in the extracts of *M. esculenta*, *H. uralum*, and *C. indicum* may indicate enhanced bioactivity, particularly in antioxidant and antimicrobial properties.

3.2. Antioxidant activity.

The antioxidant activity of the chosen seven plants was assessed and determined to vary, ranging from 40.81% in *H. uralum* to 17% in *P. americana* (Table S3). Another researcher also noted a lack of correlation between the total phenolic content and the antioxidant capacities of various medicinal plant extracts. Numerous studies have underscored the association between phenolic content and antioxidant activity [74]. For instance, Velioglu *et al*. noted a robust correlation between TPC and antioxidant activity in specific plant products [75]. Similarly, Sachdev *et al*. highlighted the role of phenolic compounds in plant defense mechanisms, specifically in mitigating the formation of reactive oxygen species (ROS) [76]. The strong antioxidant properties shown by the methanolic extracts of *M. esculenta*, *H. uralum*, and *C. indicum* were directly associated with their individual TPC levels. Nevertheless, in several other plant species, the overall phenolic content did not appear to correlate with antioxidant efficacy, despite some research suggesting a relationship between phenolic content and antioxidant capability [77]. The absence of an evident relationship between total phenolic content and antioxidant capacity in the plant extracts may reflect the possibility that the observed antioxidant activity is not solely reliant on phenolic compounds, as reported by Ispiryan et al. for *Rubus idaeus* L. Instead, it might be due to the presence of other phytochemicals, such as ascorbic acid, tocopherol, and pigments, along with their cumulative effects, all contributing to the overall antioxidant capacity [78].

3.3. Alpha-amylase inhibition activity.

The methanolic extracts of *A. adenophora*, *M. esculenta*, and *P. americana* showed IC_{50} values of 44.7±2, 75.7±1, and 113±3 µg/mL, respectively, in the alpha-amylase inhibition assay (Table 2). *A. adenophora* exhibited an inhibition of 96.58%, whereas *L. inermis* demonstrated the least inhibitory activity at 72.21% among the seven selected plants. According to a 2018 literature review by Shri, the methanolic extracts from M. esculenta leaves exhibited a hypoglycemic effect in streptozotocin-induced diabetic rats in a dose-dependent manner. The findings indicated a substantial reduction in blood glucose, cholesterol, and body weight, accompanied by a favorable effect on the lipid profile in the group that received the extract [46].

Table 2. Alpha-amylase inhibitory activity and IC_{50} of plant extracts.

S.N.	Extracts of plants (500 µg/mL)	Inhibition (%)	IC_{50} value (µg/mL)
1.	*Ageratina adenophora*	96.58	44.7 ± 2
2.	*Myrica esculenta*	95.7	75.7 ± 1
3.	*Persea americana*	87.84	113 ± 3

S.N.	Extracts of plants (500 µg/mL)	Inhibition (%)	IC_{50} value (µg/mL)
4.	*Cinnamomum glanduliferum*	78.54	113.3 ± 6
5.	*Hypericum uralum*	75.13	313.1 ± 4
6.	*Chrysanthemum indicum*	73.15	182.2 ± 2
7.	*Lawsonia inermis*	72.21	222.6 ± 3

3.4. Molecular docking scores.

The binding affinities based on a scoring function depend on factors such as the molecular weight of ligands, the size of the binding pocket, the polarity of ligands, the geometric alignment between the ligand and receptor, and the flexibility of molecules [79-81]. The higher the binding affinity, the stronger the interaction between the protein and the ligand [82]. Among several docked compounds of seven plants, several ligands achieved higher binding affinity than the native myricetin with -8.0 kcal/mol. The top five ligands based on the highest binding affinity of each plant species are shown in Table 3. The highest binding affinities were observed with Lawsonin, demonstrating an exemplary binding affinity of -10.4 kcal/mol.

Similarly, the binding affinity of -10.2 kcal/mol of lawsonic acid suggested firm binding between the receptor and the ligand molecule. Several compounds of *Lawsonia inermis*, *Chrysanthemum indicum*, *Myrica esculenta*, *Hypericum uralum*, *Persea americana*, and *Ageratina adenophora* demonstrated good binding affinity and thus hinted towards the possibility of inhibition of the HPAA. The lowest binding affinity was observed in *Cinnamomum glanduliferum*, with none of the studied ligands exhibiting binding affinity more than that of the native ligand (-8.0 kcal/mol).

Therefore, the majority of the compounds exhibited binding affinities higher than that of the native ligand and could thus inhibit the normal functioning of the HPAA enzyme.

Table 3. Binding affinity (kcal/mol) of top ligands of seven different plants with human pancreatic alpha-amylase (HPAA).

Plants	Ligands	Binding affinity (kcal/mol)
Lawsonia inermis	Lawsonin	-10.4
	Lawsonic acid	-10.2
	Lawnermis acid	-9.4
	Lawsonadeem	-9.4
	Luteolin-3-glucoside	-9.2
Myrica esculenta	Dihydroxytaraxaranoic acid	-10.0
	Dihydroxytaraxerane	-9.4
	3-epi-ursonic acid	-9.1
	Trihydroxytaraxaranoic acid	-8.9
	Myreculoside	-8.5
Chrysanthemum indicum	Quercetin-3-O-glucuronide-7-O-glucoside	-9.4
	Apigenin-7-O-rutinoside	-9.3
	Kaempferol-3-O-robinoside-7-O-rhamnoside	-9.1
	Acacetin-7-O-(6’’-O-α-L-rhamno-pyranosyl)-β-sophoroside	-9.0
	Eriodictyol-7-O-glucoside	-9.0
Hypericum uralum	Uralione E	-9.1
	Uralione I	-8.8
	Uralione H	-8.7
	Uralione F	-8.2
	Uralione B	-8.1
Persea americana	Perseapicroside A	-8.9
	Dimethyl sciadinonate	-8.3
	Dimethyl aciadinonate	-8.3
	Obovatifol	-8.1
	Obovaten	-8.1
Ageratina adenophora	Macranthoin G	-8.3
	Macranthoin F	-8.1

Plants	Ligands	Binding affinity (kcal/mol)
	chlorogenic acid methyl ester	-7.8
	7-hydroxy-8,9-dihydrothymol-9-O-trans-ferulate	-7.6
	7,8-dihydroxythymol-9-O-trans-ferulate	-7.5
Cinnamomum glanduliferum	Beta-selinene	-7.5
	Guaiazulene	-7.4
	Globulol	-7.3
	Spathulenol	-7.1
	Germacrene D-4-ol	-7.0

A lucid interactive pattern was observed between the docked ligands and the receptor. Several interactions, such as conventional hydrogen bonds, carbon-hydrogen bonds, Pi-Pi T stacked, Pi-alkyl, Pi-sigma, alkyl, van der Waals, and unfavorable donor-donor interactions, were formed between the ligands and protein molecule (Figure 1). Most of the ligands interacted with the catalytic triad: ASP197, GLU233, and ASP300 predominantly by forming the most robust non-covalent interaction, i.e., hydrogen bonds. Hydrogen bonds were also formed with amino acid residues TRP59, TYR62, ARG195, ALA198, HIS305, and ASP356. Moderate to stronger hydrogen bonds were formed in most cases. In addition to the hydrogen bonds, amino acid residues of the catalytic triad also participated in the formation of carbon-hydrogen bonds.

Furthermore, interaction with amino acid residues TRP58, TRP59, TYR62, LEU162, and LEU165 was constantly observed. LEU162 and LEU165 demonstrated interactions, such as Pi-alkyl and alkyl, involving the alkyl group of leucine with the alkyl or aromatic ring of the ligand molecules. TRP58, TRP59, and TYR62 amino acid residues interacted through the aromatic ring of the tryptophan and tyrosine amino acids, with aromaticity of the ligands forming Pi-Pi stacked or with an alkyl group forming Pi-alkyl interaction. Similarly, Pi-alkyl interactions were observed through the interaction between the Pi-bonds of HIS101, HIS201, HIS299, and HIS305, and the alkyl group of the ligand. In addition, TRP59 and TYR62 also formed a Pi-sigma bond through the interaction of the Pi-bond of the tryptophan and tyrosine ring with the sigma bond of the ligand, primarily in perseapicroside A. In contrast to all the favorable interactions, one unfavorable donor-donor interaction was found between the HIS299 amino acid residue and macranthoin G (Table 4). However, in this case, all the associating forces exceeded the disruptive force, contributing to a higher binding affinity. Several van der Waals interactions were observed between the ligand and the amino acid residues of the catalytic sites. Since interactions between the amino acid residues and the ligands were similar in the majority of the complexes, it can be inferred that the ligands were docked in the same catalytic pocket. Both hydrophilic and hydrophobic interactions were observed between the ligand molecules and the amino acid residues. The stronger binding of most ligands to the catalytic triad suggests the phytochemicals' inhibitory potential against HPAA.

Table 4. Interactions of different amino acid residues of α-amylase with compounds of selected plants based on *in vitro* assay.

Ligands	Types of interactions	Active site residues (Distance Å)
Luteolin-3-glucoside	Hydrogen Bond	TYR62 (2.49), **ASP300** (2.35)
	Carbon-hydrogen bond	**ASP197** (3.55)
	Pi-alkyl	LEU165 (5.32)
	Pi-Pi stacked	TRP59 (4.62, 5.43)
	van der Waals	TRP58, GLN63, HIS101, ARG195, ALA198, **GLU233**, ILE235, HIS299, ASP356
Lawnermis acid	Hydrogen Bond	**GLU233** (2.05)
	Pi-alkyl	TRP59 (4.67, 4.04, 5.07)
	Alkyl	LEU162 (5.02)

Ligands	Types of interactions	Active site residues (Distance Å)
	van der Waals	HIS101, THR163, LEU165, ARG195, **ASP197**, ALA198, ILE235, **ASP300**, ASP356, TRP357
Apigenin-7-O-rutinoside	Hydrogen Bond	**ASP197** (4.49), **GLU233** (1.88) HIS305 (2.42, 2.87), ASP356 (2.16)
	Carbon-hydrogen bond	**ASP300** (3.34, 3.70)
	Pi-Pi Stacked	TRP59 (4.31, 4.62, 5.72)
	van der Waals	TRP58, TRY62, GLN63, VAL98, HIS101, LEU162, THR163, LEU165, ARG195, ALA198, ILE235, GLY306
Dihydroxytaraxerane	Hydrogen Bond	TRP59 (2.47), ARG195 (1.94), **ASP197** (2.49), **GLU233** (2.30)
	Pi-alkyl	TRP58 (5.48, 5.21), TYR62 (4.12), HIS299 (5.25), HIS305 (4.59, 5.38)
	Alkyl	LEU162 (5.21)
	Pi-Sigma	TRP59 (3.74)
	van der Waals	HIS101, THR163, LEU165, ALA198, HIS201, ILE235, TRP357
3-epi-ursonic acid	Pi-alkyl	TRP59 (3.98, 4.50, 5.79)
	Alkyl	LEU162 (4.22, 5.04, 5.36), LEU165 (4.79)
	van der Waals	TRP58, TYR62, GLN63, GLY104, TYR151, ILE235
Perseapicroside A	Hydrogen Bond	**GLU233** (2.96)
	Pi-sigma	TRP59 (3.89), TYR62(4.64, 3.66)
	Pi-alkyl	TRP58 (5.43, 5.50), HIS101 (5.42), HIS299 (5.04),
	van der Waals	TYR151, LEU162, THR163, LEU165, ARG195, **ASP197**, ALA198, **ASP300**, HIS305, GLY306, ALA307
Macranthoin G	Hydrogen Bond	**GLU233** (2.09, 2.50)
	Carbon-hydrogen bond	TRP59 (3.54)
	Pi-alkyl	TRP59 (3.91, 5.65), LEU162 (5.27)
	Pi-Pi T-shaped	TYR62 (4.41)
	Unfavorable	HIS299 (2.44)
	van der Waals	GLN53, TRP58, THR163, LEU165, ARG195, **ASP197**, ALA198, HIS201, ILE235, **ASP300**, HIS305, ASP356, TRP357
Macranthoin F	Hydrogen Bond	ARG195 (2.06), ALA198 (2.83), **GLU233** (2.26)
	Carbon-hydrogen bond	TRP59 (2.45)
	Pi-alkyl	TYR62 (4.51)
	Alkyl	LEU165 (4.62)
	van der Waals	TRP58, GLN63, HIS101, LEU162, **ASP197**, HIS201, ILE235, HIS299, **ASP300**

Overall, the binding interactions were primarily driven by hydrogen bonds involving the catalytic triad and adjacent polar residues. Additionally, hydrophobic forces, such as Pi-alkyl, alkyl, and π-π stacking, played a crucial role in stabilizing ligand-receptor complexes, particularly for ligands containing aromatic or alkyl groups. These findings highlight that both hydrophilic and hydrophobic characteristics of the ligands are essential contributors to their binding affinity.

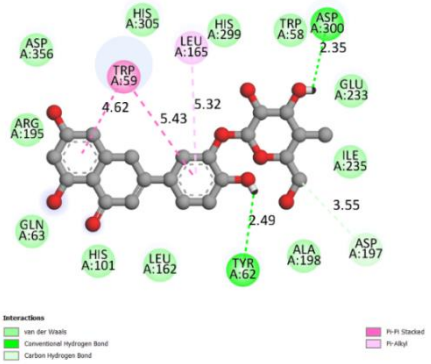

(a)

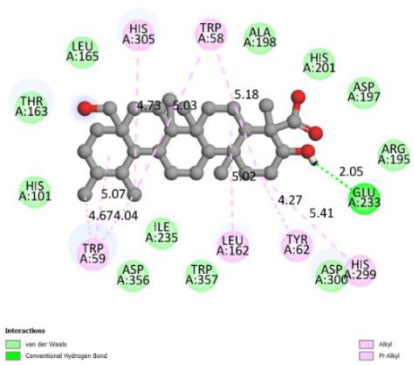

(b)

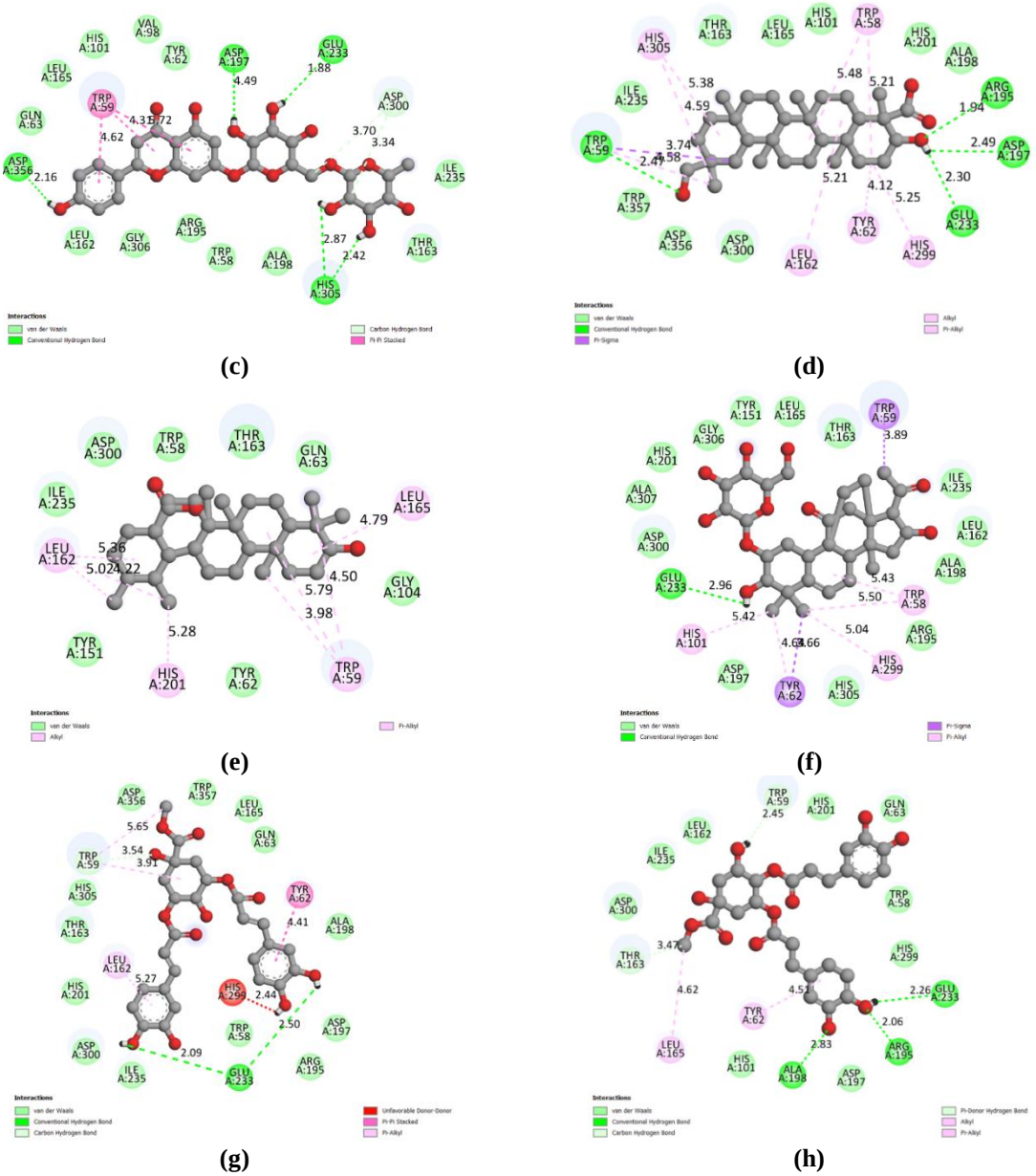

Figure 1. 2D interaction of **(a)** Luteolin-3-glucoside; **(b)** Lawnermis acid; **(c)** Apigenin-7-O-rutinoside; **(d)** Dihydroxytaraxerane; **(e)** 3-epi-ursonic acid; **(f)** Perseapicroside A; **(g)** Macranthoin G; **(h)** Macranthoin F with α-amylase.

3.5. Geometrical descriptions from MDS.

3.5.1. Root mean square deviation (RMSD).

The geometrical stability of the complex was assessed through MDS [83]. The RMSD profile obtained from the MDS helps to evaluate the stability of the protein-ligand complex over time [84]. From the results of numerous compounds of seven plants, only eight compounds of five plants (*Lawsonia inermis*, *Chrysanthemum indicum*, *Myrica esculenta*, *Persea americana*, and *Ageratina adenophora*) exhibited good to moderate stability with HPAA, along with an acceptable RMSD of the ligand better than that of the native ligand (Figure S2).

Two compounds, namely luteolin and lawnermis acid, exhibited almost identical RMSD values below 6 Å. Despite a few peaks and bumps at *ca.* 60 and 70 ns, the luteolin-amylase system attained equilibrium after 120 ns, with a smooth RMSD trajectory of

approximately 4 Å, indicating system stability. Similarly, the lawnermic-amylase system also remained equilibrated for the last 25 ns (Figure 2A). From the selected compounds, apigenin-7-O-rutinoside-amylase complex demonstrated excellent stability with an RMSD of the ligand below *ca.* 3.5 Å throughout a 200 ns production run, without any spikes or bumps on the curve (Figure 2B). Two compounds, namely, dihydroxytaraxerane and 3-epi-ursonic acid, showed significant stability despite relatively higher RMSD values of around 6 Å and 9 Å, respectively. In the case of 3-epi-ursonic acid, the ligand shifted its docked position around 10 ns, and after several adjustments, the ligand remained stable after 40 ns, with a remarkably smooth trajectory until the end (Figure 2C).

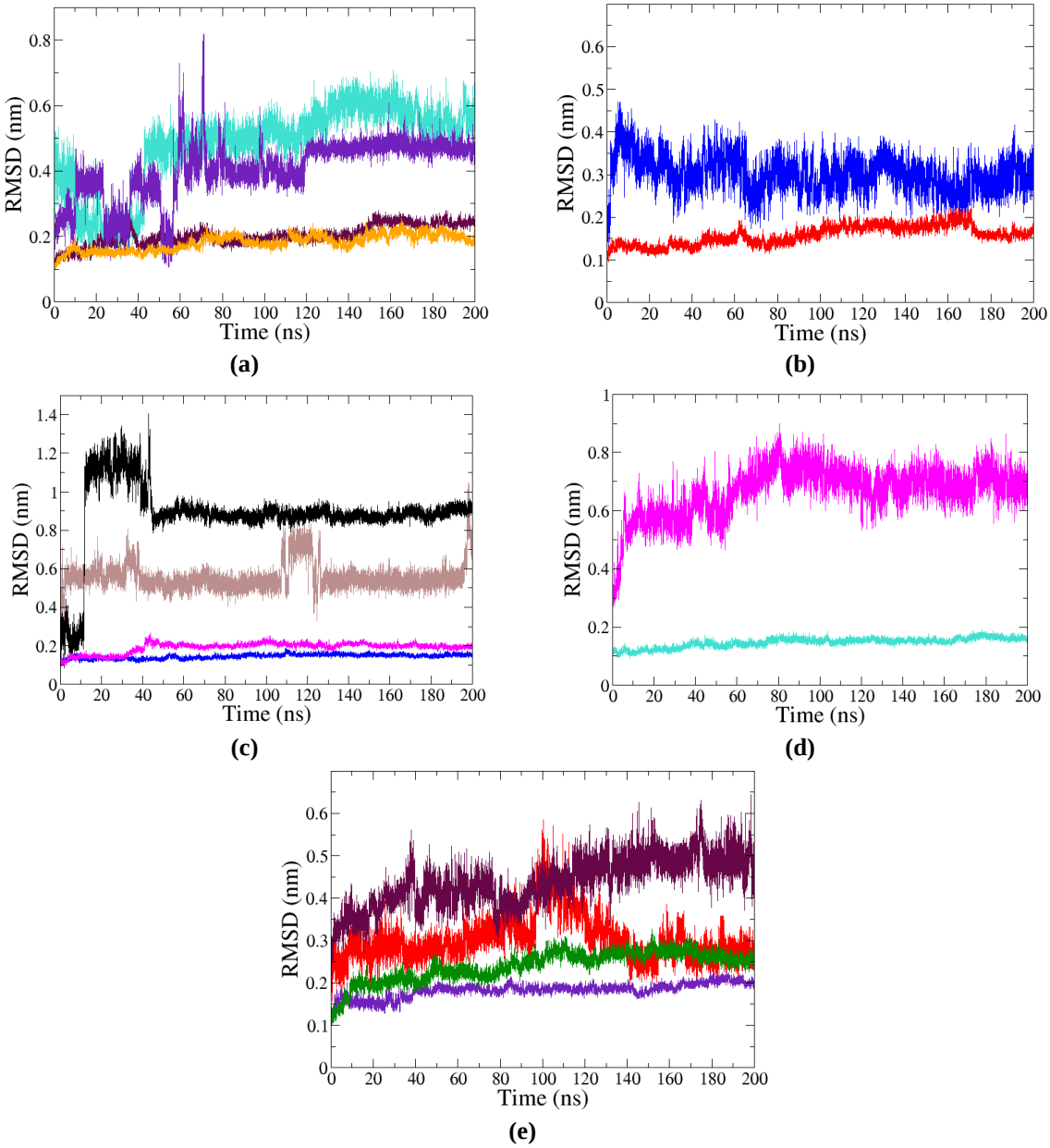

Figure 2. RMSD of **(a)** Luteolin-3-glucoside (violet), and Lawnermis acid (turquoise) with respect to protein backbone in Luteolin-3-glucoside complex (orange) and Lawnermis acid complex (maroon); **(b)** Apigenin-7-O-rutinoside (blue) with respect to protein backbone (red); **(c)** Dihydroxytaraxerane (brown) and 3-epi-ursonic acid (black) with respect to protein backbone of Dihydroxytaraxerane complex (magenta) and 3-epi-ursonic acid (blue); **(d)** Perseapicroside A (magenta) with respect to protein backbone of Perseapicroside A-complex (turquoise); **(e)** Macranthoin G (red) and Macranthoin F (maroon) with respect to protein backbone of Macranthoin G complex (green) and Macranthoin F complex (indigo).

Similarly, perseapicroside A demonstrated stable complex formation with an RMSD of approximately 7 Å (Figure 2D). In contrast, two compounds, macranthoin G and

macranthoin F, exhibited good RMSD values below 5 Å. The RMSD of macranthoin G showed stability with a smooth trajectory consistently below 3 Å, except for a slight rise up to 5.5 Å at 100-120 ns (Figure 2E). Furthermore, the RMSD profile of the protein backbone in all the complexes at approximately 2.5 Å and below indicated the stability of protein structure upon ligand binding (Figure S3). The RMSD values for all ligands relative to the protein backbone indicate that the complexes were stable and could thus inhibit the protein's normal function.

3.5.2. Root mean square fluctuation (RMSF).

The RMSF plot was used to examine how the alpha-carbon atoms of amino acid residues within the protein fluctuate from their average positions upon ligand binding [85].

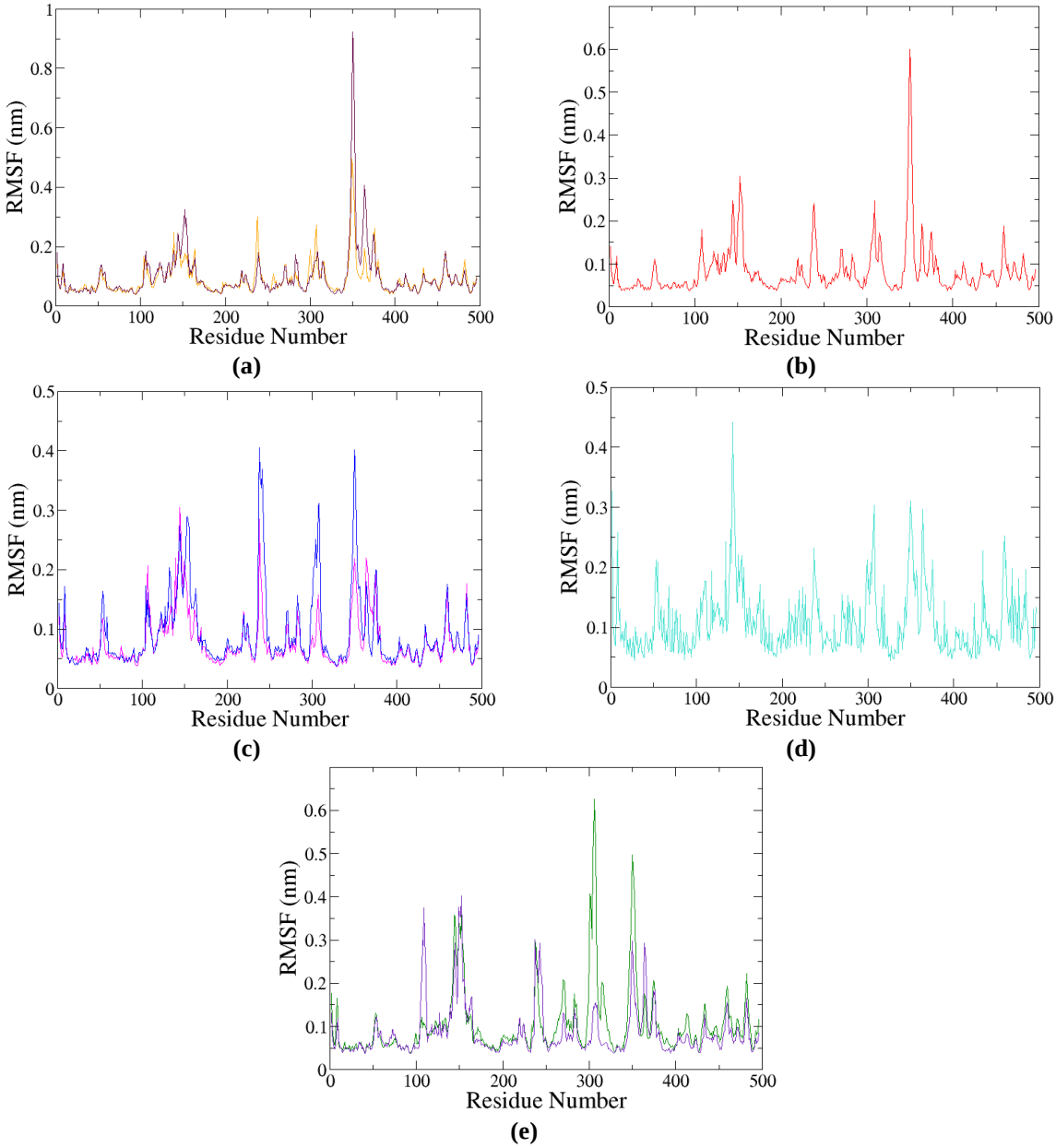

Figure 3. RMSF of **(a)** Luteolin-3-glucoside complex (orange) and Lawnermis acid complex (maroon); **(b)** Apigenin-7-O-rutinoside complex (red); **(c)** Dihydroxytaraxerane complex (magenta), and 3-epi-ursonic acid complex (blue); **(d)** Perseapicroside A-complex (turquoise); **(e)** Macranthoin G complex (green) and Macranthoin F complex (indigo).

The RMSF plots show lower fluctuations in the catalytic triad (ASP197, GLU233, and ASP300) of the protein compared to the apo structure, indicating the protein's stability upon

ligand binding, as shown in Figure 3 and Figure S4. Additionally, ligand binding reduced fluctuations in amino acid residues near the catalytic pocket. The larger spikes at around 150 and 350 amino acid residues were due to a highly mobile, unstable, and fluctuating loop structure located more than 15 Å from the active site. Similar results in RMSF of α-amylase have been reported in recent MD simulation studies [86-88]. The fluctuation of these amino acid residues at a large distance from the catalytic pocket does not affect the ligand binding, and the adduct remains intact. Among all the complexes, perseapicroside A-complex showed slightly unusual fluctuation in each amino acid residue.

Despite different ligands binding with the receptor, the observed RMSF values were almost similar for most of the complexes. Lower fluctuation at the catalytic triad suggested strong binding of the ligand at the active site. This would ensure that the protein backbone and its conformation remain intact, strengthening the adduct's stability.

3.5.3. Radius of gyration (R_g).

The distance of each atom from the central axis of the protein molecule was assessed in terms of radius of gyration (R_g).

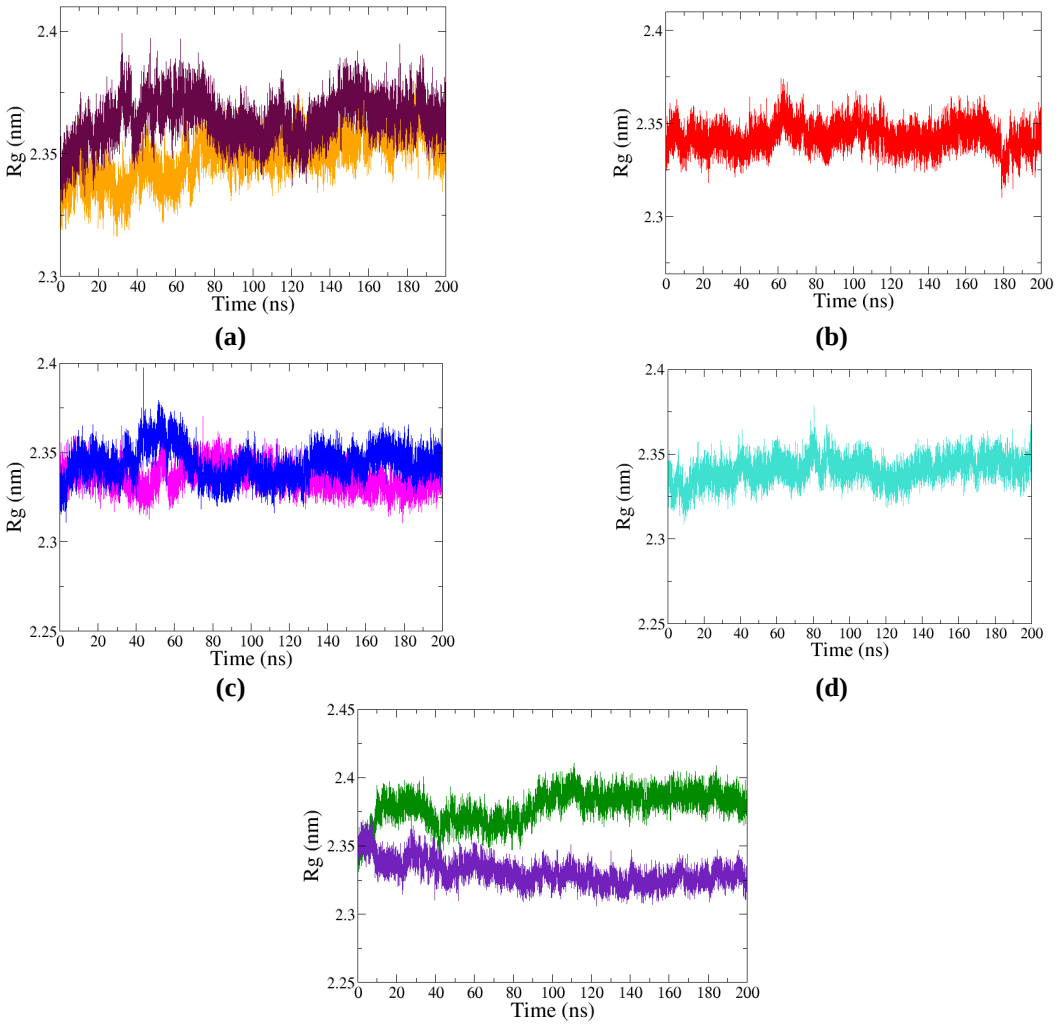

Figure 4. R_g profile of **(a)** Luteolin-3-glucoside complex (orange) and Lawnermis acid complex (maroon); **(b)** Apigenin-7-O-rutinoside complex (red); **(c)** Dihydroxytaraxerane complex (magenta) and 3-epi-ursonic acid complex (blue); **(d)** Perseapicroside A-complex (turquoise); **(e)** Macranthoin G complex (green) and Macranthoin F complex (indigo).

Smooth trajectories with average R_g at approximately 23.5±0.5 Å were observed with luteolin-3-glucoside, lawnermis acid, apigenin-7-O-rutinoside, dihydroxytaraxerane, 3-epi-ursonic acid, and perseapicroside A (Figure 4), comparable with the apostructure (Figure S5). The mean R_g values for macranthoin G and macranthoin F were approximately 23.2 Å and 23.7 Å, respectively. An analogous R_g value for α-amylase at around 23.5±3 Å aligns with that reported in the previous work [87, 88]. The stable and smooth R_g trajectories for all complexes suggest no observable expansion and compression of the protein structure upon ligand binding. This provided insight into conformational changes such as compressibility and expandability of the protein structure [89].

3.5.4. Solvent accessible surface area (SASA).

SASA was utilized to evaluate the geometrical stability of protein structure by assessing the solvent-accessible or wettable portion of the protein [90]. An average SASA of 200±10 nm^2 was consistently observed for luteolin-3-glucoside, lawnermis acid, apigenin-7-O-rutinoside, dihydroxytaraxerane, perseapicroside A, and macranthoin F complexes throughout the 200 ns simulation.

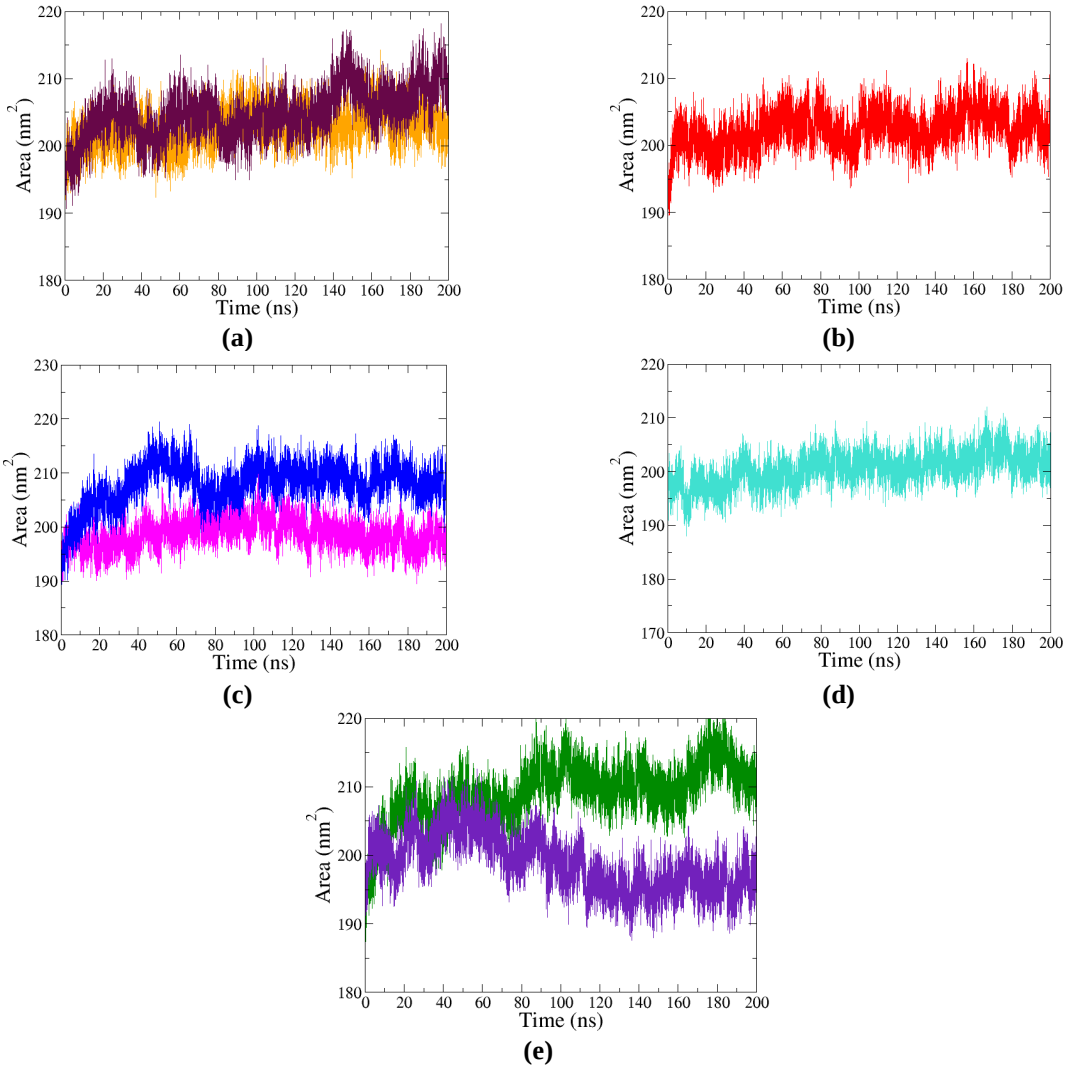

Figure 5. SASA of **(a)** Luteolin-3-glucoside complex (orange) and Lawnermis acid complex (maroon); **(b)** Apigenin-7-O-rutinoside complex (red); **(c)** Dihydroxytaraxerane complex (magenta) and 3-epi-ursonic acid complex (blue); **(d)** Perseapicroside A-complex (turquoise); **(e)** Macranthoin G complex (green) and Macranthoin F complex (indigo).

The mean SASA value was about 210±10 nm^2 for 3-epi-ursonic acid and macranthoin G complexes (Figure 5). The SASA of the apostructure is shown in Figure S6. Lower SASA values indicate strong ligand binding within the protein's orthosteric pocket, contributing to protein compactness [91, 92]. Conversely, higher values indicate protein tertiary structure distortion. The consistent SASA value of approximately 210 nm^2 observed for most complexes, with slight variations for macranthoin F and macranthoin G, suggests minimal change in the protein's solvent-accessible surface area. This implies that the protein's hydrophobic region remained shielded from solvent, thereby preserving the stability of the protein backbone [93, 94].

3.5.5. Chemistry with hydrogen bonds.

The stability of the complex is determined by the number of hydrogen bonds formed between the ligand and the protein [95]. An inversely proportional relationship between the RMSD of ligands and the number of hydrogen bonds can be observed, as depicted in Figures 2 and 6 [96].

A relatively lower number of hydrogen bonds was observed for luteolin-3-glucoside and lawnermis acid (Figure 6A and 6B). In the case of luteolin, the number of hydrogen bonds decreased from 8 to 4 and remained constant. The plunge in hydrogen bonds to a minimum of two at 70 ns could have resulted in sharp peaks in the RMSD of the ligand at the same instant. Apigenin-7-O-rutinoside exhibited a more significant number of hydrogen bonds with α-amylase. It consistently formed six to seven hydrogen bonds, with eight hydrogen bonds formed during a few instances. The consistent number of hydrogen bonds might have contributed to the smooth RMSD of ligands below 4 Å, as depicted in Figure 6C. Moderate (three to four hydrogen bonds) and relatively lower (two to three hydrogen bonds) counts were observed in dihydroxytaraxerane complex and 3-epi-ursonic acid, respectively (Figure 6D and 6E). The moderate to low hydrogen bond count may have resulted in a relatively higher RMSD than in other complexes. The drop in the number of hydrogen bonds from 110 to 120 ns could have led to the sudden spikes observed in the RMSD curve (up to 8 Å) during the same simulation period (110 to 120 ns).

Perseapicroside A exhibited a relatively higher number of hydrogen bonds, reaching a maximum of seven. The number of hydrogen bonds remained consistent with five to six after 60 ns, correlating with the stable RMSD of the ligand after 60 ns (Figure 6F). The highest number of hydrogen bonds, a maximum of nine for macrathoin G (Figure 6G) and a maximum of eight for macranthoin F (Figure 6H), were observed.

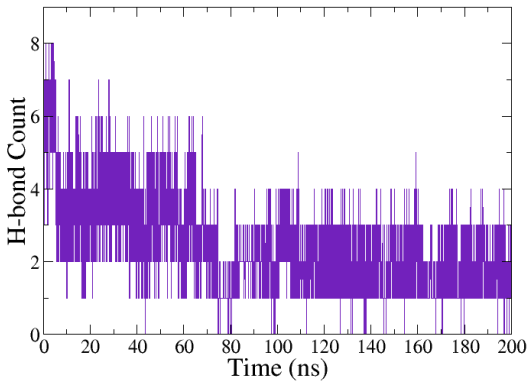

(a)

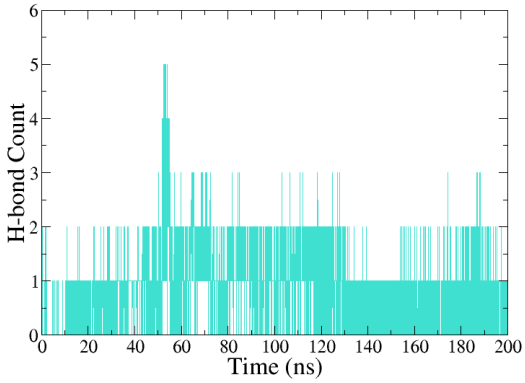

(b)

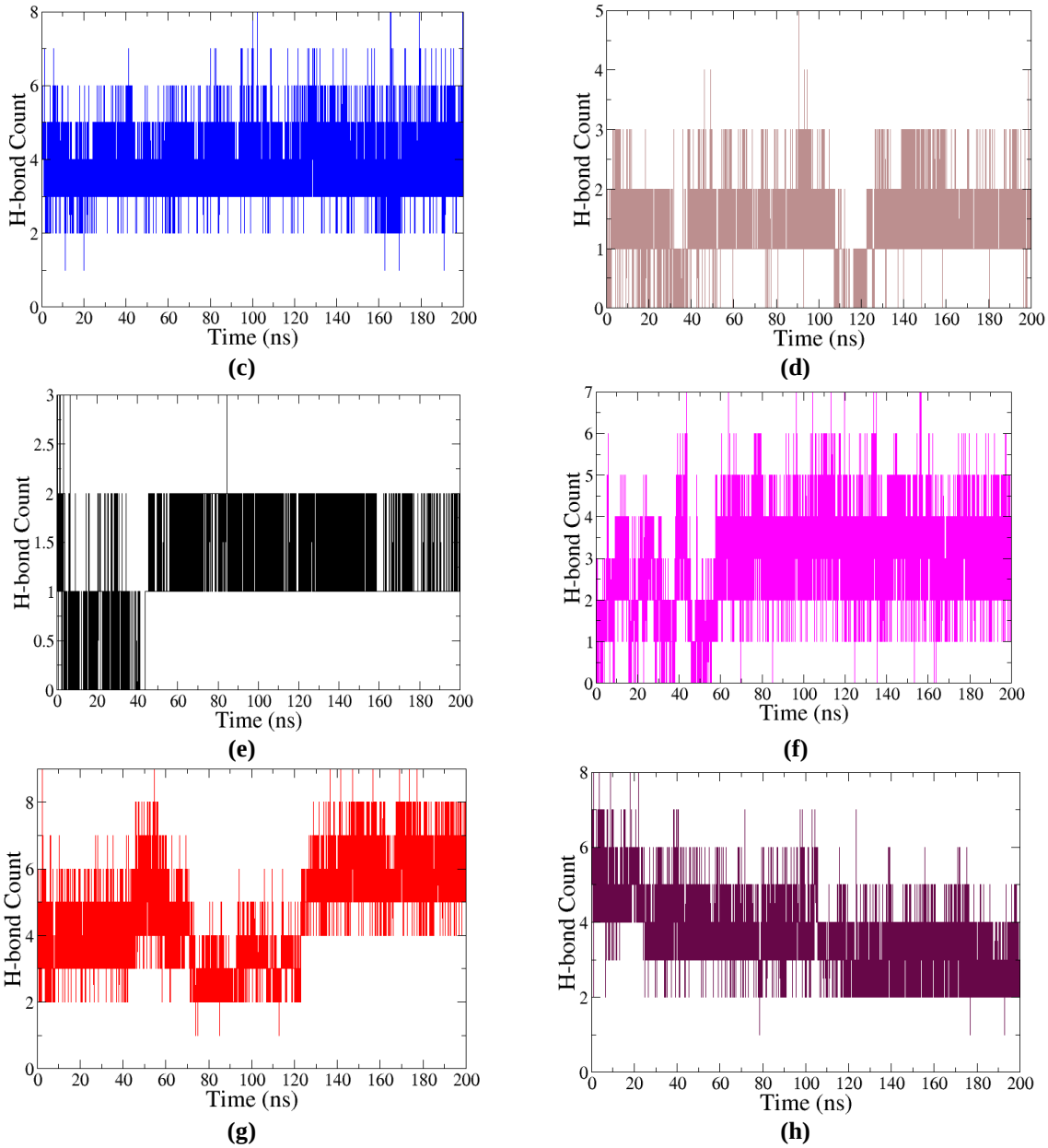

Figure 6. Number of hydrogen bonds of **(a)** Luteolin-3-glucoside (violet); **(b)** Lawnermis acid (turquoise); **(c)** Apigenin-7-O-rutinoside (blue); **(d)** Dihydroxytaraxerane (brown); **(e)** 3-epi-ursonic acid (black); **(f)** Perseapicroside A (magenta); **(g)** Macranthoin G (red); **(h)** Macranthoin F (maroon).

In the macranthoin G complex, eight hydrogen bonds were formed continuously within the simulation period, thus reducing the RMSD of the ligand below 3 Å and demonstrating relatively higher stability among the studied compounds. The decrease in hydrogen bond count from 80 ns to 120 ns might account for the slight increase in the ligand's RMSD. Moreover, the slightly increasing RMSD curve of the ligand of macranthoin F could be attributed to the moderately decreasing trend of the number of hydrogen bonds in macranthoin F.

3.5.6. Binding free energy changes (ΔG_{BFE}).

The spontaneity and feasibility of the adduct formation reactions were assessed through the binding free energy changes (ΔG_{BFE}) [97]. A more negative binding energy change indicates greater thermodynamic stability of the complex. The binding free energies for all complexes were negative, indicating that complex formation was spontaneous. The highest (ΔG_{BFE}) was observed with macranthoin G at -42.51±7.17 kcal/mol, demonstrating remarkable

thermodynamic stability of the system. Likewise, binding free energy changes of -39.58±3.57 kcal/mol, -35.92±4.95 kcal/mol, -29.67±3.93 kcal/mol, -27.93±2.69 kcal/mol, and -23.73±2.96 kcal/mol were observed with macranthoin F, apigenin-7-O-rutinoside, perseapicroside A, lawnermis acid, dihydroxytaraxerane complex, luteolin-3-glucoside, and 3-epi-ursonic acid, respectively (Table 5). While frame-by-frame ΔG_{BFE} of the equilibrated part of the trajectory suggested the system was stable for the specific time frame, as seen in Figure S7, the average negative ΔG_{BFE} inferred that the overall complex formation was generally spontaneous. The change in free energy with frames indicates the spontaneity of the forward reaction and implies that the values remain negative throughout the simulation period.

Table 5. Change in binding free energy (kcal/mol) of adducts with different components for 20 ns from the MMPBSA approach.

Complex	$\Delta E_{VDWAALS}$	ΔE_{EL}	ΔE_{PB}	ΔE_{NPOLAR}	ΔG_{GAS}	ΔG_{SOLV}	ΔG_{BFE}
Apigenin-7-O-rutinoside	45.73± 3.70	-70.91± 10.54	86.20± 7.81	-5.48± 0.20	-116.54± 10.07	80.72± 7.70	-35.92± 4.95
Luteolin-3-glucoside	-34.66± 3.15	-31.45± 5.63	46.97± 5.36	-4.00± 0.19	-66.11± 5.82	42.97± 5.27	-23.14± 3.43
Lawnermis acid	-49.26± 2.45	-6.16± 3.06	32.14± 3.14	-4.65± 0.13	-55.42± 3.79	27.49± 3.12	-27.93± 2.69
Dihydroxytaraxerane	-30.40± 2.80	-20.97± 4.28	32.46± 3.65	-3.82± 0.12	-51.37± 3.95	28.64± 3.62	-23.73± 2.96
3-epi-ursonic acid	-40.88± 3.00	-16.83± 4.01	41.09± 4.75	-5.00± 0.09	-57.72± 4.18	36.09± 4.58	-21.63± 5.08
Perseapicroside A	-43.12± 2.95	-22.55± 6.33	40.54± 4.82	-4.53± 0.09	-65.67± 6.69	36.00± 4.80	-29.67± 3.93
Macranthoin G	-35.01± 4.17	-93.51± 6.81	90.98± 7.02	-4.97± 0.12	-128.52± 6.69	86.01± 6.98	-42.51± 7.17
Macranthoin F	-32.95± 3.92	-50.87± 5.91	48.72± 5.22	-4.48± 0.19	-83.82± 7.00	44.24± 5.14	-39.58± 3.57

To strengthen the mechanistic understanding, the study integrated experimental α-amylase inhibition data with in silico docking and molecular dynamics simulations. Phytochemicals showing notable *in vitro* inhibitory activity, such as those from Ageratina adenophora and Myrica esculenta, also demonstrated strong binding affinities and stable interactions with key catalytic residues in computational analyses. This correlation was further supported by stable RMSD profiles, consistent hydrogen bonding, and favorable binding free energy values observed during simulations. The convergence of experimental and computational results highlights the potential of these compounds to inhibit α-amylase through direct interaction with its active site. However, as *in silico* findings are predictive, further validation through detailed enzyme kinetics and crystallographic studies is essential to confirm these interactions and their therapeutic relevance.

4. Conclusions

Sixteen plants with traditional medicinal significance were tested for their bioactive properties, and 7 were found to possess α-amylase inhibitory activity. These plants were characterized for TPC, TFC, antioxidant properties, and alpha-amylase inhibition, and 122 phytochemicals present in them were subjected to computational studies for molecular-level insights. The selected 8 molecules from 5 plants, *C. indicum*, *M. esculenta*, *A. adenophora*, *L. inermis*, and *P. americana* showed better binding scores than that of the native ligand. The spatial and thermodynamic stability derived from the molecular dynamics simulation was found to be acceptable. The binding free energy changes suggested that the forward reaction for the formation of the adduct from the ligand and receptor was spontaneous at the equilibrated

part of the trajectory. The hit molecules could potentially disrupt or inhibit the normal functioning of α-amylase, which would help to control diabetes. The synergy between experimental and computational outcomes paves the way for further characterization to develop the molecules as effective, safe, drug-like candidates.

Extensive molecular dynamics simulations demonstrated that the compounds can form stable protein-ligand complexes both structurally and thermodynamically under physiological conditions. These results support future experimental validation and pharmacological research, highlighting their potential for developing safer, more effective diabetes therapies derived from natural products. As next steps, *in vivo* validation, toxicity screening, and dose-optimization studies will be essential to confirm their efficacy and safety profiles.

Author Contributions

Conceptualization, B.P.M, J.A.S., and R.L.S.S.; methodology, B.P.M, P.G., P.N., M.P. T.M.; software, B.M., T.S., S.B.; validation, B.P.M, P.N., and M.P.; formal analysis, B.P.M., P.G., T.M.; investigation, P.G., P.N., M.P.; resources, B.M., T.S., S.B.; data curation, B.P.M., P.G., and T.M.; writing- original draft preparation, B.P.M, P.N., M.P.; writing- review and editing, J.A.S., R.L.S.S. All authors have read and agreed to the published version of the manuscript.

Institutional Review Board Statement

Not applicable.

Informed Consent Statement

Not applicable.

Data Availability Statement

All the data supporting the findings of the study are presented in the main manuscript and the supplementary file.

Funding

This research received no external funding.

Acknowledgments

The authors thank Kathmandu Valley College, Kathmandu, Nepal, for the computational resources.

Conflicts of Interest

The authors declare no conflict of interest.

References

1. Mishra, S.; Tiwari, P.; Yadav, R.; Patel, P.S. An Extensive Analysis of Diseases Associated with Diabetes. *J. Pharma Insights Res.* **2024**, *2*, 174–187, https://doi.org/10.69613/ng1j7s13.
2. American Diabetes Association. Diagnosis and classification of diabetes mellitus. Diabetes Care. *Am. Diabetes Assoc*. **2014**, *37*, S81–90, https://doi.org/10.2337/dc14-S081.

3. King, H.; Aubert, R.E.; Herman, W.H. Global burden of diabetes, 1995–2025: Prevalence, numerical estimates, and projections. *Diabetes Care* **1998**, *21*, 1414–1431, https://doi.org/10.2337/diacare.21.9.1414.
4. Ahmed, A.; Shetty, P.; Shetty, G.B. Sun-dried tomato powder reduces blood sugar levels and improves the lipid profile among people with type-2 diabetes : A randomized controlled trial. *World Nutr.* **2024**, *15*, 71–77, https://doi.org/10.26596/wn.202415471-77.
5. Liu, Y.; Jia, Y.; Wu, Y.; Zhang, H.; Ren, F.; Zhou, S. Review on mechanisms of hypoglycemic effects of compounds from highland barley and potential applications. *Food Funct.* **2024**, *15*, 11365–11382, https://doi.org/10.1039/D4FO00940A.
6. Khan, F.; Khan, M. V.; Kumar, A.; Akhtar, S. Recent advances in the development of alpha-glucosidase and alpha-amylase inhibitors in type 2 diabetes management: Insights from in silico to in vitro studies. *Curr. Drug Targets* **2024**, *25*, 782–795, https://doi.org/10.2174/0113894501313365240722100902.
7. Dhankhar, S.; Mahajan, S.; Chauhan, S.; Saini, M.; Garg, N.; Singh, T.G. Herbal DPP-4 Inhibitors: Comprehensive Review of their Effectiveness, Safety and Environmental Fate in Diabetes Mellitus. *Curr. Bioact. Compd.* **2024**, *21*, e15734072322250, https://doi.org/10.2174/0115734072322250240924081053.
8. Dai, J.; Ting, H.; Xiaodie, H.; Huaying, L.; Lintong, L.; Jie, S.; Jie, P.; Cheng, Ji. Evaluating Preferences of Hospitalized Diabetes Patients for Hospital-Wide Glycemic Control Programme: A Discrete Choice Experiment. *J. Diabetes Res.* **2024**, *2024*, 2552658, https://doi.org/10.1155/2024/2552658.
9. Shukia, R.; Sharma, S.B.; Puri, D.; Prabhu, K.M.; Murthy, P.S. Medicinal plants for treatment of diabetes mellitus. *Indian J. Clin. Biochem.* **2000**, *15*, 169–177, https://doi.org/10.1007/BF02867556.
10. Menichetti, F.; Berteotti, C.; Schirinzi, V.; Poli, C.; Arrighi, R.; Leone, A. Moringa oleifera and blood pressure: Evidence and potential mechanisms. *Nutrients* **2025**, *17*, 1258, https://doi.org/10.3390/nu17071258.
11. Aryal, D.; Soniya, J.; Thapa, N.K.; Chaudhary, P.; Basaula, S.; Joshi, U.; Bhandari, D. *et al*. Dietary phenolic compounds as promising therapeutic agents for diabetes and its complications: A comprehensive review. *Food Sci. Nutr.* **2024**, *12*, 3025–3045, https://doi.org/10.1002/fsn3.3983.
12. Bauer, I.; Gerald, R.; Sönke, C.; Anja, B.W.; Julian, W.; Ignacio, R. I.; Kai, L. A comprehensive in-vitro/in-vivo screening toolbox for the elucidation of glucose homeostasis modulating properties of plant extracts (from roots) and its bioactives. *Front. Pharmacol.* **2024**, *15*, 1396292, https://doi.org/10.3389/fphar.2024.1396292.
13. Kumari, V. B. C.; Huligere, S.S.; Ahmed, M.Z.; Ramu, R. Fermented Ananas comosus and Carica papaya harbour putative probiotic Limosilactobacillus fermentum and Lacticaseibacillus paracasei strains with inhibitory activity against α-glucosidase and α-amylase. *S. Afr. J. Bot.* **2024**, *172*, 348–360, https://doi.org/10.1016/j.sajb.2024.07.022.
14. Shahidi, F.; Danielski, R. Review on the role of polyphenols in preventing and treating type 2 diabetes: Evidence from in vitro and in vivo studies. *Nutrients* **2024**, *16*, 3159, https://doi.org/10.3390/nu16183159.
15. Ouma, R. B. O.; Ngari, S. M.; Kibet, J. K. A review of the current trends in computational approaches in drug design and metabolism. *Discov. Public Health* **2024**, *21*, 108, https://doi.org/10.1186/s12982-024-00229-3.
16. Bettanti, A.; Beccari, A. R.; Biccarino, M. Exploring the future of biopharmaceutical drug discovery: can advanced AI platforms overcome current challenges?. *Discov. Artif. Intell.* **2024**, *4*, 102, https://doi.org/10.1007/s44163-024-00188-3.
17. Duraipandiyan, V.; Ayyanar, M.; Ignacimuthu, S. Antimicrobial activity of some ethnomedicinal plants used by Paliyar tribe from Tamil Nadu, India. *BMC Complement. Altern. Med.* **2006**, *6*, 35, https://doi.org/10.1186/1472-6882-6-35.
18. Ainsworth, E.A.; Gillespie, K.M. Estimation of total phenolic content and other oxidation substrates in plant tissues using folin–ciocalteu reagent. *Nat. Protoc.* **2007**, *2*, 875–877, https://doi.org/10.1038/nprot.2007.102.
19. Lu, X.; Wang, J.; Al-Qadiri, H.M.; Ross, C.F.; Powers, J.R.; Tang, J.; Rasco, B.A. Determination of total phenolic content and antioxidant capacity of onion (Allium cepa) and shallot (Allium oschaninii) using infrared spectroscopy. *Food Chem.* **2011**, *129*, 637-644, https://doi.org/10.1016/j.foodchem.2011.04.105.
20. Chang, C.-C.; Yang, M.-H.; Wen, H.-M.; Chern, J.-C. Estimation of total flavonoid content in propolis by two complementary colometric methods. *J. Food Drug Anal.* **2002**, *10*, 178-182, https://doi.org/10.38212/2224-6614.2748.
21. Senger, M.R.; Gomes L da, C.A.; Ferreira, S.B.; Kaiser, C.R.; Ferreira, V.F.; Silva, F.P. Kinetics studies on the inhibition mechanism of pancreatic α-amylase by glycoconjugated 1H-1,2,3-triazoles: A new class

of inhibitors with hypoglycemiant activity. *ChemBioChem*. **2012**, *13*, 1584–1593, https://doi.org/10.1002/cbic.201200272.
22. Kang, S.C.; Lim, S.Y.; Song, Y.J. Lupeol is one of active components in the extract of Chrysanthemum indicum Linne that inhibits LMP1-induced NF-κB activation. *PLoS One* **2013**, *8*, e82688, https://doi.org/10.1371/journal.pone.0082688.
23. Tian, D.; Yang, Y.; Yu, M.; Han, Z.Z.; Wei, M.; Zhang, H.W. *et al*. Anti-inflammatory chemical constituents of: Flos Chrysanthemi Indici determined by UPLC-MS/MS integrated with network pharmacology. *Food Funct*. **2020**, *11*, 6340–6351, https://doi.org/10.1039/D0FO01000F.
24. Shao, Y.; Sun, Y.; Li, D.; Chen, Y. Chrysanthemum indicum L.: A Comprehensive Review of its Botany, Phytochemistry and Pharmacology. *Am. J. Chinese. Med*. **2020**, *48*, 871-897, https://doi.org/10.1142/S0192415X20500421.
25. Luyen, B.T.T.; Tai, B.H.; Thao, N.P.; Lee, Y.M.; Lee, S.H.; Jang, H.D. *et al*. The anti-osteoporosis and antioxidant activities of chemical constituents from chrysanthemum indicum flowers. *Phyther. Res*. **2015**, *29*, 540–548, https://doi.org/10.1002/ptr.5281.
26. Siddiqui, B.S.; Kardar, M.N.; Ali, S.T.; Khan, S. Two new and a known compound from Lawsonia inermis Asia. *Helv. Chim. Acta*. **2003**, *86*, 2164–2169, https://doi.org/10.1002/hlca.200390174.
27. Chaudhary, G.; Goyal, S.; Poonia, P. Linn L. Lawsonia inermis Linnaeus : A Phytopharmacological Review. *Int. J. Pharm. Sci. Drug Res*. **2010**, *2*, 91–98, https://doi.org/10.25004/IJPSDR.2010.020202.
28. Kamal, M.; Jawaid, T. Pharmacological activities of lawsonia inermis Linn.: a review. *Int. J. Biomed. Res.* **2010**, *1*, 37-43, https://doi.org/10.7439/ijbr.v1i2.56.
29. Hsouna A.B.; Trigui, M.; Culioli, G.; Blache, Y.; Jaoua, S. Antioxidant constituents from Lawsonia inermis leaves: Isolation, structure elucidation and antioxidative capacity. *Food Chem*. **2011**, *125*, 193–200, https://doi.org/10.1016/j.foodchem.2010.08.060.
30. Li, Q.; Gao, W.; Cao, J.; Bi, X.; Chen, G.; Zhang, X.; Xia, X.; Zhao, Y. New cytotoxic compounds from flowers of Lawsonia inermis L. *Fitoterapia* **2014**, *94*, 148-154, https://doi.org/10.1016/j.fitote.2014.02.007.
31. Semwal, R.B.; Semwal, D.K.; Combrinck, S.; Cartwright-Jones, C.; Viljoen, A. Lawsonia inermis L. (henna): Ethnobotanical, phytochemical and pharmacological aspects. *J. Ethnopharmacol*. **2014**, *155*, 80–103, https://doi.org/10.1016/j.jep.2014.05.042.
32. Singh, D.K.; Luqman, S.; Mathur, A.K. Lawsonia inermis L. - A commercially important primaeval dying and medicinal plant with diverse pharmacological activity: A review. *Ind. Crops Prod*. **2015**, *65*, 269–286, https://doi.org/10.1016/j.indcrop.2014.11.025.
33. Moutawalli, A.; Benkhouili, F.Z.; Doukkali, A.; Benzeid, H.; Zahidi, A. The biological and pharmacologic actions of Lawsonia inermis L. *Phytomedicine Plus*. **2023**, *3*, 100468, https://doi.org/10.1016/j.phyplu.2023.100468.
34. Zhou, Z.B.; Li, Z.R.; Wang, X.B.; Luo, J.G.; Kong, L.Y. Polycyclic polyprenylated derivatives from Hypericum uralum: Neuroprotective effects and antidepressant-like activity of Uralodin A. *J. Nat. Prod*. **2016**, *79*, 1231–1240, https://doi.org/10.1021/acs.jnatprod.5b00667.
35. Subba, B.; Kandel, R.C. Chemical composition and bioactivity of essential oil of Ageratina adenophora from Bhaktapur district of Nepal J. *Nepal Chem. Soc*. **2012**, *30*, 78-86, https://doi.org/10.3126/jncs.v30i0.9350.
36. Zhang, M.; Liu, W.X.; Zheng, M.F.; Xu, Q.L.; Wan, F.H.; Wang, J. *et al*. Bioactive quinic acid derivatives from Ageratina adenophora. *Molecules* **2013**, *18*, 14096–14104, https://doi.org/10.3390/molecules181114096.
37. Giri, S.; Sahu, R.; Paul, P.; Nandi, G.; Dua, T.K. An updated review on Eupatorium adenophorum Spreng. [Ageratina adenophora (Spreng.)]: traditional uses, phytochemistry, pharmacological activities and toxicity. *Pharmacol. Res. Mod. Chin. Med*. **2022**, *2*, 100068, https://doi.org/10.1016/j.prmcm.2022.100068.
38. Dong, L.-M.; Zhang, M.; Xu, Q.-L.; Zhang, Q.; Luo, B.; Luo, Q.-W.; Liu, W.-B.; Tan, J.-W. Two new thymol derivatives from the roots of Ageratina adenophora. *Molecules* **2017**, *22*, 592, https://doi.org/10.3390/molecules22040592.
39. Zheng, G.; Luo, S.; Li, S.; Hua, J.; Li, W.; Li, S. Specialized metabolites from Ageratina adenophora and their inhibitory activities against pathogenic fungi. *Phytochemistry* **2018**, *148*, 57–62, https://doi.org/10.1016/j.phytochem.2018.01.013.

40. André, R.; Catarro, J.; Freitas, D.; Pacheco, R.; Oliveira, M.C.; Serralheiro, M.L.; Falé, P.L. Action of euptox A from Ageratina adenophora juice on human cell lines: A top-down study using FTIR spectroscopy and protein profiling. *Toxicol. In Vitro* **2019**, *57*, 217-225, https://doi.org/10.1016/j.tiv.2019.03.012.
41. Poudel, R.; Neupane, N.P.; Mukeri, I.H. An updated review on invasive nature, phytochemical evaluation, and pharmacological activity of Ageratina adenophora. *Artic Int. J. Pharm. Sci. Res*. **2020**, *11*, 2510-2520.
42. Bhuyan, D.J.; Alsherbiny, M.A.; Perera, S.; Low, M.; Basu, A.; Devi, O.A.; Barooah, M.S.; Li, C.G.; Papoutsis, K. The odyssey of bioactive compounds in avocado (Persea americana) and their health benefits. *Antioxidants* **2019**, *8*, 426, https://doi.org/10.3390/antiox8100426.
43. Ngbolua, K te N. A mini-review on the phytochemistry and pharmacology of the medicinal plant species Persea americana Mill. (Lauraceae). *Discov. Phytomedicine* **2019**, *6*, https://doi.org/10.15562/phytomedicine.2019.99.
44. Nhiem, N.X.; Van Kiem, P.; Van Minh, C.; Tai, B.H.; Cuong, N.X.; Thu, V.K.; Anh, H.L.T.; Jo, S.-H.; Jang, H.-D.; Kwon, Y.-I. A new monoterpenoid glycoside from Myrica esculenta and the inhibition of angiotensin I-converting enzyme. *Chem. Pharm. Bull.* **2010**, *58*, 1408-1410, https://doi.org/10.1248/cpb.58.1408.
45. Khanal, A.; Raut, B.; Khanal, D.P.; Koirala, N. Bioactivity evaluations from stem bark extract fractions of Myrica esculenta Buch. -Ham.ex D. Don. *Food Safe Health* **2024**, *2*, 480-488, https://doi.org/10.1002/fsh3.12063.
46. Shri, R.; Sood, P. A review on ethnomedicinal, phytochemical and pharmacological aspects of Myrica esculenta. *Indian J. Pharm. Sci*. **2018**, *80*, 2-13, https://doi.org/10.4172/pharmaceutical-sciences.1000325.
47. Prashar, Y.; Patel, N.J. A review on Myrica Nagi: Approach in recognizing the overall potential of the plant. **2018**, *4*, 217–31, https://doi.org/10.26479/2018.0406.16.
48. Kabra, A.; Martins, N.; Sharma, R.; Kabra, R.; Baghel, U.S. Myrica esculenta Buch.-Ham. ex D. Don: A natural source for health promotion and disease preventdion. *Plants* **2019**, *8*, 149, https://doi.org/10.3390/plants8060149.
49. Shrivastava, A.K.; Chaudhary, D.; Shrestha, L.; Awadalla, M.E.; Al-Shouli, S.T.; Palikhey, A.; Eltayb, W.A.; Gupta, A.; Gupta, P.P.; Parab, M.; *et al*. GC-MS Based Metabolite Profiling, and Anti-Inflammatory Activity of Aqueous Extract of *Myrica esculenta* through *In Vitro* and *In Silico* Approach. *Med. Sci. Forum* **2023**, *21*, 52, https://doi.org/10.3390/ECB2023-14079.
50. Baruah, A.; Nath, S.C. Leaf essential oils of Cinnamomum glanduliferum (wall) meissn and Cinnamomum glaucescens (nees) meissn. *J. Essent. Oil Res*. **2006**, *18*, 200–222, https://doi.org/10.1080/10412905.2006.9699065.
51. Thantsin, K.; Zhang, Q.; Yang, J.; Wang, Q. Composition of semivolatile compounds of 10 Cinnamomum species from China and Myanmar. *Nat. Prod. Res*. **2008**, *22*, 576–583, https://doi.org/10.1080/14786410701592802.
52. Singh, C.; Singh, S.; Pande, C.; Tewari, G.; Kharkwal, G.C. Chemical composition of the leaves essential oil from Cinnamomum glanduliferum (Wall) Meissn from Uttarakhand, India. *J. Essent. Oil-Bearing Plants*. **2014**, *17*, 927–930, https://doi.org/10.1080/0972060X.2014.935027.
53. Taha, A.S.M.; Eldahshan, O.A. Chemical characteristics, antimicrobial, and cytotoxic activities of the essential oil of Egyptian Cinnamomum glanduliferum bark. *Chem. Biodivers*. **2017**, *14*, e1600443, https://doi.org/10.1002/cbdv.201600443.
54. Azaba, S.S.; Abdel Jaleelb, G.A.; Eldahshanc, O.A. Anti-inflammatory and gastroprotective potential of leaf essential oil of Cinnamomum glanduliferum in ethanol-induced rat experimental gastritis. *Pharm. Biol*. **2017**, *55*, 1654–1661, https://doi.org/10.1080/13880209.2017.1314512.
55. Li, Z.; Wan, H.; Shi, Y.; Ouyang, P. Personal experience with four kinds of chemical structure drawing software: review on ChemDraw, ChemWindow, ISIS/Draw, and ChemSketch. *J. Chem. Inf. Model*. **2004**, *44*, 1886-1890, https://doi.org/10.1021/ci049794h.
56. Hanwell, M.D.; Curtis, D.E.; Lonie, D.C.; Vandermeerschd, T.; Zurek, E.; Hutchison, G.R. Avogadro: An advanced semantic chemical editor, visualization, and analysis platform. *J. Cheminform*. **2012**, *4*, 17, https://doi.org/10.1186/1758-2946-4-17.
57. Trott, O.; Olson, A.J. AutoDock Vina: Improving the speed and accuracy of docking with a new scoring function, efficient optimization, and multithreading. *J. Comput. Chem*. **2009**, *31*, 455-461, https://doi.org/10.1002/jcc.21334.
58. Berman, H.M.; Westbrook, J.; Feng, Z.; Gilliland, G.; Bhat, T.N.; Weissig, H.; Shindyalov, I.N.; Bourne, P.E. The protein data bank. *Nucleic Acids Res.* **2000**, *28*, 235-242, https://doi.org/10.1093/nar/28.1.235.

59. Waterhouse, A.; Bertoni, M.; Bienert, S.; Studer, G.; Tauriello, G.; Gumienny, R.; Heer, F.T.; de Beer, T.A.P.; Rempfer, C.; Bordoli, L. SWISS-MODEL: homology modelling of protein structures and complexes. *Nucleic Acids Res.* **2018**, *46*, W296-W303, https://doi.org/10.1093/nar/gky427.
60. Ramírez, D.; Caballero, J. Is it reliable to take the molecular docking top scoring position as the best solution without considering available structural data?. *Molecules* **2018**, *23*, 1038, https://doi.org/10.3390/molecules23051038.
61. Jain, A.N. Surflex: Fully automatic flexible molecular docking using a molecular similarity-based search engine. *J. Med. Chem*. **2003**, *46*, 499–511, https://doi.org/10.1021/jm020406h.
62. Li, X.; Li, Y.; Cheng, T.; Liu, Z.; Wang, R. Evaluation of the performance of four molecular docking programs on a diverse set of protein-ligand complexes. *J. Comput. Chem*. **2010**, *31*, 2109–2125, https://doi.org/10.1002/jcc.21498.
63. Abraham, M.J.; Murtola, T.; Schulz, R.; Páll, S.; Smith, J.C.; Hess, B.; Lindahl, E. GROMACS: High performance molecular simulations through multi-level parallelism from laptops to supercomputers. *SoftwareX* **2015**, *1-2*, 19-25, https://doi.org/10.1016/j.softx.2015.06.001.
64. Foloppe, N.; Mackerell, A.D. All-atom empirical force field for nucleic acids: I. parameter optimization based on small molecule and condensed phase macromolecular target data all-atom empirical force field for nucleic acids. *Int. J. Comput. Chem*. **2000**, *21*, 86–104, https://doi.org/10.1002/(SICI)1096-987X(20000130)21:2<86::AID-JCC2>3.0.CO;2-G.
65. Zoete, V.; Cuendet, M.A.; Grosdidier, A.; Michielin, O. SwissParam: A fast force field generation tool for small organic molecules. *J. Comput. Chem*. **2011**, *32*, 2359–2368, https://doi.org/10.1002/jcc.21816.
66. Valdés-Tresanco, M.S.; Valdés-Tresanco, M.E.; Valiente, P.A.; Moreno, E. Gmx_MMPBSA: A new tool to perform end-state free energy calculations with GROMACS. *J. Chem. Theory Comput*. **2021**, *17*, 6281–6291, https://doi.org/10.1021/acs.jctc.1c00645.
67. Dong, L.; Qu, X.; Zhao, Y.; Wang, B. Prediction of binding free energy of protein-ligand complexes with a hybrid molecular mechanics/generalized born surface area and machine learning method. *ACS Omega* **2021**, *6*, 32938–32947, https://doi.org/10.1021/acsomega.1c04996.
68. Tripathi, Y.C.; Saini, N. Total phenolic, total flavonoid content and antioxidant efficacy of leaves of eupatorium adenophorum. *Int. J. Pharma. Bio. Sci*. **2019**, *10*, 157-166, https://doi.org/10.22376/ijpbs.2019.10.2.p157-166.
69. Regmi, S.; Sharma, K.R. Determination of total phenolic and flavonoid content, antidiabetic, and antioxidant activities of leaves and seeds extracts of Eucalyptus robusta Sm. and Ageratina adenophora Spreng. *J. Nepal. Chem. Soc*. **2023**, *43*, 171-179, https://doi.org/10.3126/jncs.v43i2.53817.
70. Stratil, P.; Klejdus, B.; Kubáň, V. Determination of total content of phenolic compounds and their antioxidant activity in vegetables-Evaluation of spectrophotometric methods. *J. Agric. Food Chem*. **2006,** *54*, 607–616, https://doi.org/10.1021/jf052334j.
71. Doshi, P.; Adsule, P.; Banerjee, K. Phenolic composition and antioxidant activity in grapevine parts and berries (Vitis vinifera L.) cv. Kishmish Chornyi (Sharad Seedless) during maturation. *Int. J. Food Sci. Technol*. **2006**, *41*, 1–9, https://doi.org/10.1111/j.1365-2621.2006.01214.x.
72. Kapali, J.; Sharma, K.R. Estimation of phytochemicals, antioxidant, antidiabetic and brine shrimp lethality activities of some medicinal plants growing in Nepal. *Central Dept. Chem*. **2021**, *20*, 102–116, https://doi.org/10.52547/jmp.20.80.102.
73. Kabra, A.; Sharma, R.; Hano, C.; Kabra, R.; Martins, N.; Baghel, U.S. Phytochemical composition, antioxidant, and antimicrobial attributes of different solvent extracts from Myrica esculenta Buch.-Ham. ex. D. Don leaves. *Biomolecules* **2019**, *9*, 357, https://doi.org/10.3390/biom9080357.
74. Rawat, S.; Jugran, A.; Giri, L.; Bhatt, I.D.; Rawal, R.S. Assessment of antioxidant properties in fruits of Myrica esculenta : A popular wild edible species in Indian himalayan region. *Evid Based Complement. Alternat Med.* **2011**, *2011*, 512787, https://doi.org/10.1093/ecam/neq055.
75. Velioglu, Y.S.; Mazza, G.; Gao, L.; Oomah, B.D. Antioxidant activity and total phenolics in selected fruits, vegetables, and grain products. *J. Agric. Food Chem*. **1998,** *46*, 4113–4117, http://dx.doi.org/10.1021/jf9801973.
76. Sachdev, S.; Ansari, S.A.; Ansari, M.I.; Fujita, M.; Hasanuzzaman, M. Abiotic stress and reactive oxygen species: Generation, signaling, and defense mechanisms. *Antioxidants* **2021**, *10*, 277, https://doi.org/10.3390/antiox10020277.
77. Yang, J-H.; Lin, H-C.; Mau, J-L. Antioxidant properties of several commercial mushrooms. *Food Chem.* **2002**, *77*, 229–235, https://doi.org/10.1016/S0308-8146(01)00342-9.

78. Ispiryan, A.; Vilma, A.; Natalija, M.; Antanas, S.; Alvija, S.; Dalia, U.; Jonas, V.; Rasa, P.; Lina, R. Correlation between Antimicrobial Activity Values and Total Phenolic Content/Antioxidant Activity in Rubus idaeus L. *Plants* **2024**, *13*, 504, https://doi.org/10.3390/plants13040504.
79. Wang, H. Prediction of protein–ligand binding affinity via deep learning models. *Brief. Bioinform.* **2024**, *25*, bbae081, https://doi.org/10.1093/bib/bbae081.
80. Patil, V.M.; Gupta, S.P.; Masand, N.; Balasubramanian, K. Experimental and computational models to understand protein-ligand, metal-ligand and metal-DNA interactions pertinent to targeted cancer and other therapies. *Eur. J. Med. Chem. Rep.* **2024**, *10*, 100133, https://doi.org/10.1016/j.ejmcr.2024.100133.
81. Wang, Z.; Zhou, F.; Wang, Z.; Hu, Q.; Li, Y.-Q.; Wang, S.; Wei, Y.; Zheng, L.; Li, W.; Peng, X. Fully flexible molecular alignment enables accurate ligand structure modeling. *J. Chem. Inf. Model.* **2024**, *64*, 6205-6215, https://doi.org/10.1021/acs.jcim.4c00669.
82. Du, X.; Li, Y.; Xia, Y.-L.; Ai, S.-M.; Liang, J.; Sang, P.; Ji, X.-L.; Liu, S.-Q. Insights into protein–ligand interactions: mechanisms, models, and methods. *Int. J. Mol. Sci.* **2016**, *17*, 144, https://doi.org/10.3390/ijms17020144.
83. Adcock, S.A.; McCammon, J.A. Molecular dynamics: Survey of methods for simulating the activity of proteins. *Chem. Rev*. **2006**, *106*, 1589–615, https://doi.org/10.1021/cr040426m.
84. Salo-Ahen, O.M.; Alanko, I.; Bhadane, R.; Bonvin, A.M.; Honorato, R.V.; Hossain, S.; Juffer, A.H.; Kabedev, A.; Lahtela-Kakkonen, M.; Larsen, A.S. Molecular dynamics simulations in drug discovery and pharmaceutical development. *Processes* **2020**, *9*, 71, https://doi.org/10.3390/pr9010071.
85. Martínez, L. Automatic identification of mobile and rigid substructures in molecular dynamics simulations and fractional structural fluctuation analysis. *PLoS One* **2015**, *10*, e0119264, https://doi.org/10.1371/journal.pone.0119264.
86. Ahmed, S.; Ali, M.C.; Ruma, R.A.; Mahmud, S.; Paul, G.K.; Saleh, M.A.; Alshahrani, M.M.; Obaidullah, A.J.; Biswas, S.K.; Rahman, M.M. Molecular docking and dynamics simulation of natural compounds from betel leaves (Piper betle L.) for investigating the potential inhibition of alpha-amylase and alpha-glucosidase of type 2 diabetes. *Molecules* **2022**, *27*, 4526, https://doi.org/10.3390/molecules27144526.
87. Sharma, P.; Joshi, T.; Joshi, T.; Chandra, S.; Tamta, S. Molecular dynamics simulation for screening phytochemicals as α-amylase inhibitors from medicinal plants. *J. Biomol. Struct. Dyn*. **2021**, *39*, 6524–6538, https://doi.org/10.1080/07391102.2020.1801507.
88. Abchir, O.; Daoui, O.; Belaidi, S.; Ouassaf, M.; Qais, F.A.; ElKhattabi, S.; Belaaouad, S.; Chtita, S. Design of novel benzimidazole derivatives as potential α-amylase inhibitors using QSAR, pharmacokinetics, molecular docking, and molecular dynamics simulation studies. *J. Mol. Model.* **2022**, *28*, 106, https://doi.org/10.1007/s00894-022-05097-9.
89. Lobanov, M.Y.; Bogatyreva, N.S.; Galzitskaya, O. V. Radius of gyration as an indicator of protein structure compactness. *Mol. Biol*. **2008**, *42*, 623–628, https://doi.org/10.1134/S0026893308040195.
90. Durham, E.; Dorr, B.; Woetzel, N.; Staritzbichler, R.; Meiler, J. Solvent accessible surface area approximations for rapid and accurate protein structure prediction. *J. Mol. Model*. **2009**, *15*, 1093–1108, https://doi.org/10.1007/s00894-009-0454-9.
91. Raut, B.K.; Upadhyaya, S.R.; Bashyal, J.; Parajuli, N. In silico and in vitro analyses to repurpose quercetin as a human pancreatic α-amylase inhibitor. *ACS Omega* **2023**, *8*, 43617–43631, https://doi.org/10.1021/acsomega.3c05082.
92. Ashraf, N.; Asari, A.; Yousaf, N.; Ahmad, M.; Ahmed, M.; Faisal, A.; Saleem, M.; Muddassar, M. Combined 3D-QSAR, molecular docking and dynamics simulations studies to model and design TTK inhibitors. *Front. Chem.* **2022**, *10*, 1003816, https://doi.org/10.3389/fchem.2022.1003816.
93. Zhang, D.; Lazim, R. Application of conventional molecular dynamics simulation in evaluating the stability of apomyoglobin in urea solution. *Sci. Rep*. **2017**, *7*, 44651, https://doi.org/10.1038/srep44651.
94. Lolok, N.; Sumiwi, S.A.; Muhtadi, A.; Susilawati, Y.; Hendriani, R.; Ramadhan, D.S.F.; Levita, J.; Sahidin, I. Molecular docking and molecular dynamics studies of bioactive compounds contained in noni fruit (Morinda citrifolia L.) against human pancreatic α-amylase. *J. Biomol. Struct. Dyn.* **2022**, *40*, 7091-7098, https://doi.org/10.1080/07391102.2021.1894981.
95. Tayyeb, J.Z.; Mondal, S.; Anisur Rahman, M.; Kumar, S.; Bayıl, I.; Akash, S.; Hossain, M.S.; Alqahtani, T.; Zaki, M.E.; Oliveira, J.I.N. Identification of Helicobacter pylori-carcinogenic TNF-alpha-inducing protein inhibitors via daidzein derivatives through computational approaches. *J. Cell. Mol. Med*. **2024**, *28*, e18358, https://doi.org/10.1111/jcmm.18358.

96. Kony, D.B.; Hünenberger, P.H.; Gunsteren van, W.F. Molecular dynamics simulations of the native and partially folded states of ubiquitin: Influence of methanol cosolvent, pH, and temperature on the protein structure and dynamics. *Protein Sci*. **2007**, *16*, 1101–1118, https://doi.org/10.1110/ps.062323407.
97. Cournia, Z.; Allen, B.; Sherman, W. Relative binding free energy calculations in drug discovery: Recent advances and practical considerations. *J. Chem. Inf. Model*. **2017**, *57*, 2911–2937, https://doi.org/10.1021/acs.jcim.7b00564.
98. Dhital, S.; Parajuli, N.; Poudel, M.; Shrestha, T.; Bharati, S.; Maharjan, B.; Marasini, B.P.; Adhikari Subin, J.; Shrestha R.L.S. Spatial and Energetic Stability Assessment of the Adducts of Phytocompounds of Piper longum L. with α -amylase by Computational Approach. *Biointerface Res. Appl. Chem.* **2024**, *14*, 126, https://doi.org/10.33263/BRIAC146.126.

Supplementary Information

Lawsonia inermis

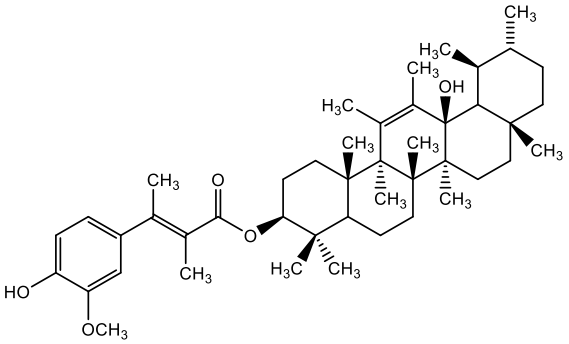

Lawsonin

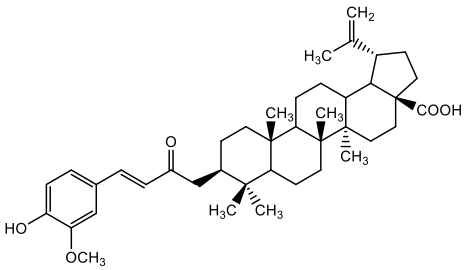

Lawsonic acid

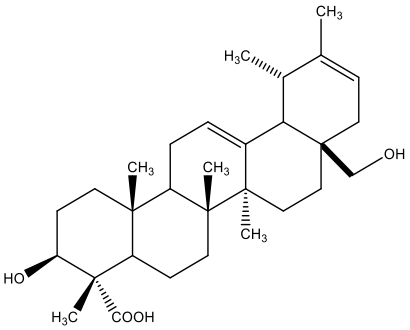

Lawnermis acid

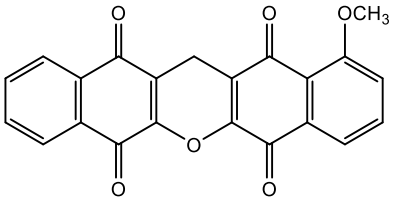

Lawsonadeem

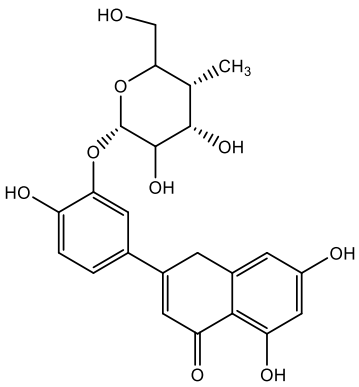

Luteolin-3-glucoside

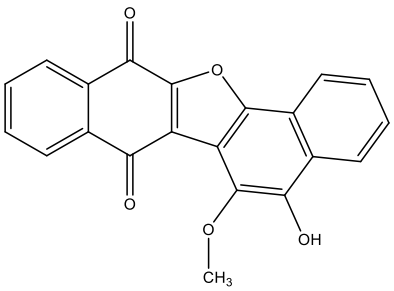

Balsaminone A

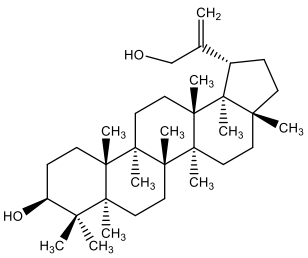

Hennadiol

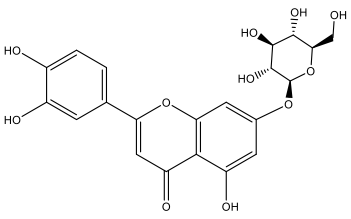

luteolin-7-O-β-D-glucopyranoside

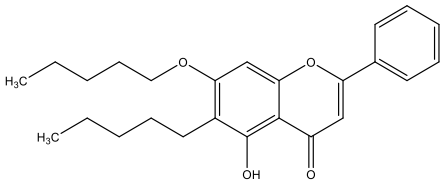

Lawsochrysin

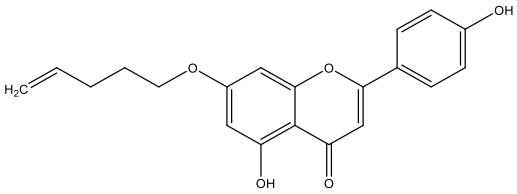

Lawsonaringenin

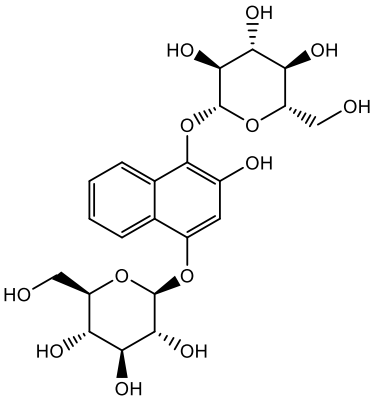

Lawsoniaside

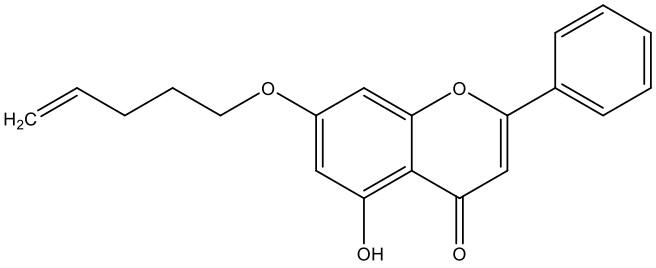

Lawsochrysinin

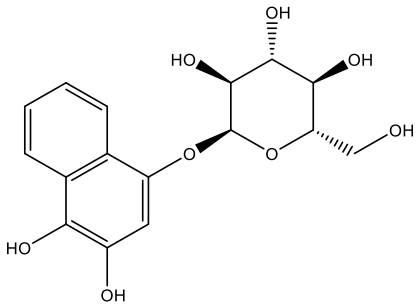

1,2-Dihydroxy-4-O-glucosyloxynaphthalene

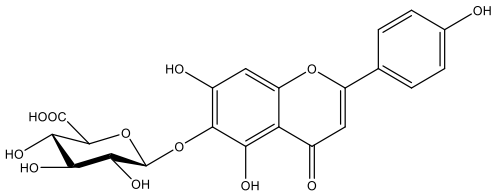

Isocutellarin

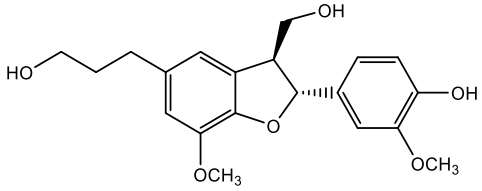

Dihydrodehydrodiconyferyl alcohol

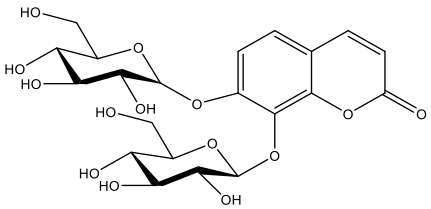

Daphneside

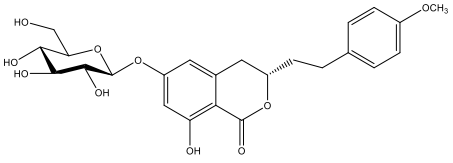

Agrimonolide 6-O-β-D-glucopyranoside

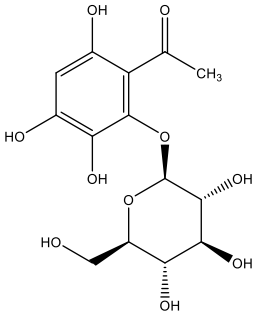

Lalioside

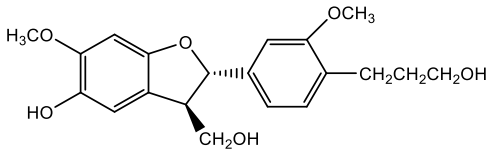

Lawsonicin

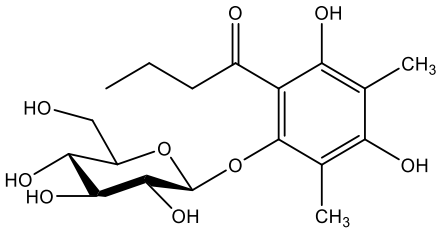

Lawsoniaside A

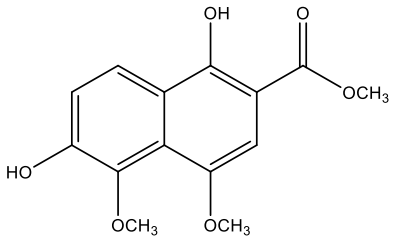

Lawsonaphthoate C

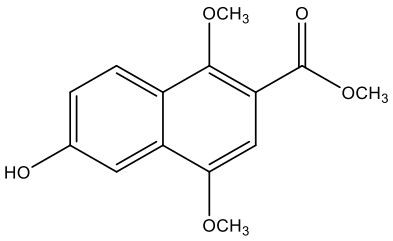

Lawsonaphthoate B

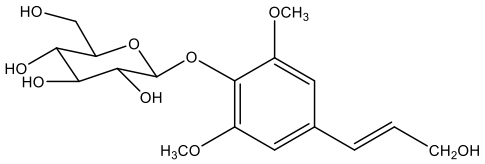

Lawsoniaside B

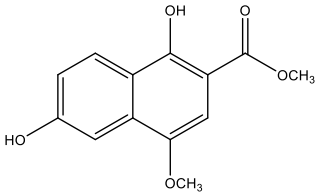

Lawsonaphthoate A

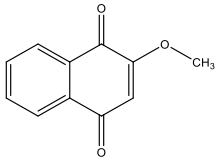

2-Methoxy-3-methyl-1,4-naphthaquinone

Chrysanthemum indicum

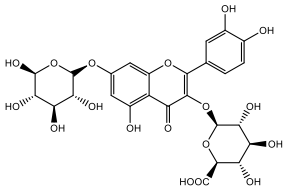

Quercetin-3-O-glucuronide-7-O-glucoside

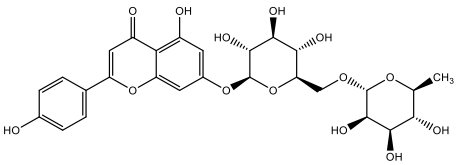

Apigenin-7-O-rutinoside

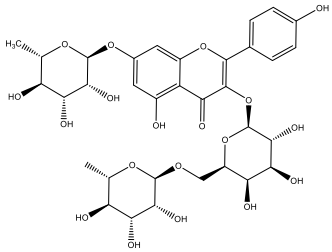

Kaempferol-3-O-robinoside-7-O-rhamnoside

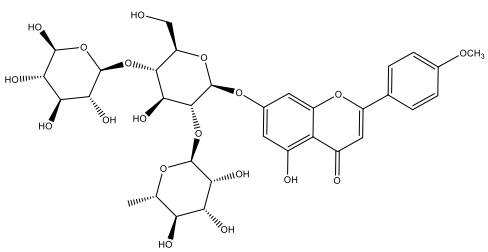

pyranosyl)-β-

Acacetin-7-O-(6’’-O-α-L-rhamno-sophoroside

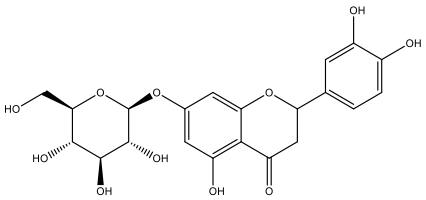

Eriodictyol-7-O-glucoside

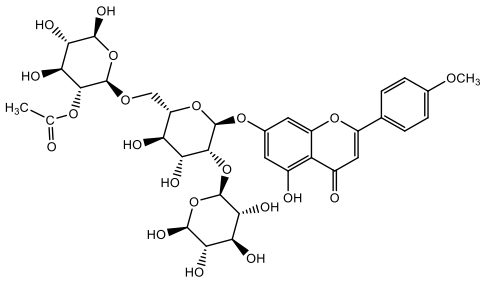

Acacetin-7-O-β-D-rhamnopyranosyl-(1→6)-[2-O-acetyl-glucopyranosyl (1→2)] glucopyranoside

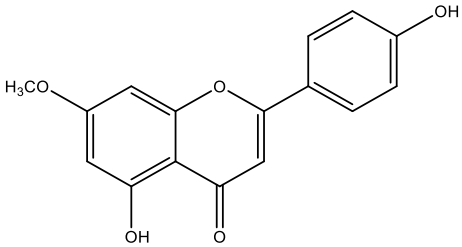

5,4'-Dihydroxy-7-methoxyflavone

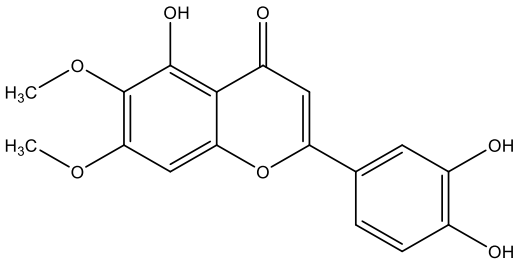

5,3',4'-Trihydroxy-6,7-dimethoxyflavone

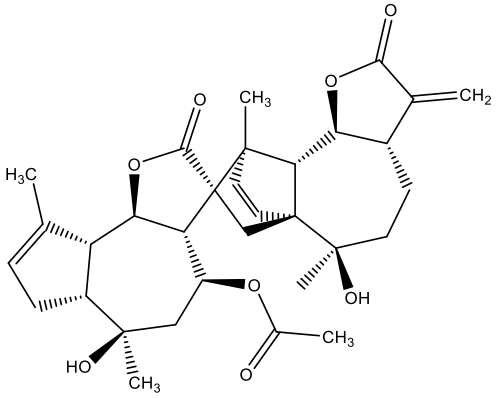

Handelin

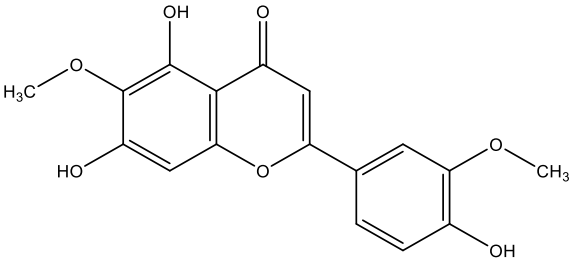

Jaceosidin

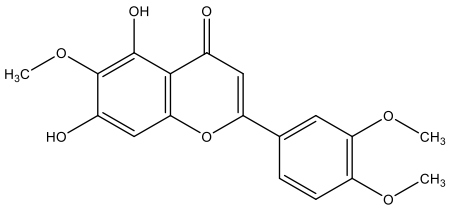

Eupatolitin

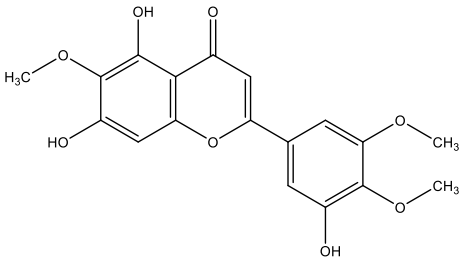

5,7,3'-Trihydroxy-6,4',5'-trimethoxyflavone

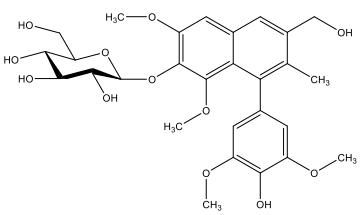

Chrysanthelignanoside A

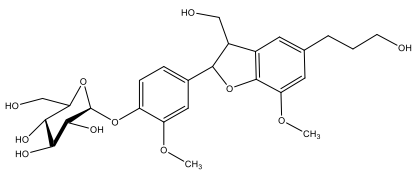

urolignoside

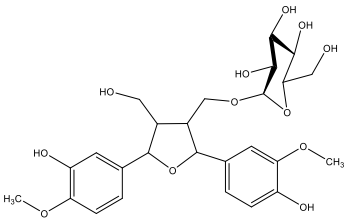

(7R,7’R,8S,8’S)-neo-olivil-9-O-β-D-glucopyranoside

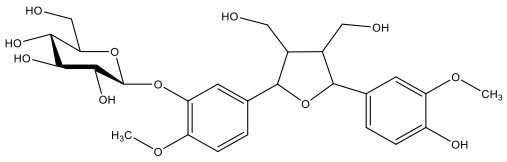

(7R,7’R,8S,8’S)-neo-olivil-4-O-b-D-glucopyranoside

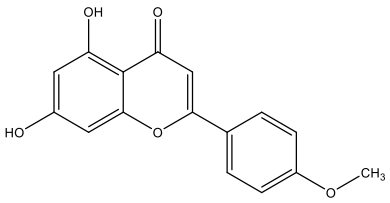

Acacetin

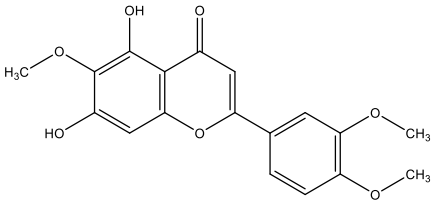

Eupatilin

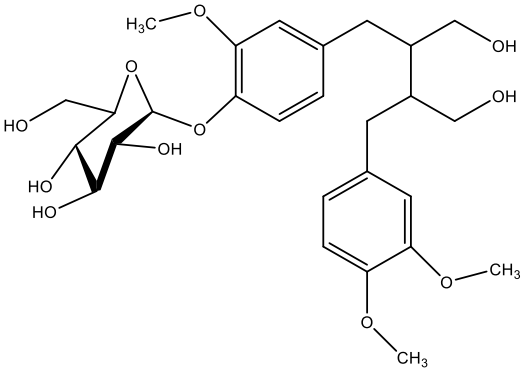

secoisolariciresinol-4-O-β-D-glucopyranoside

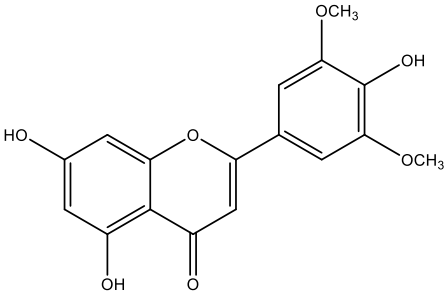

Tricin

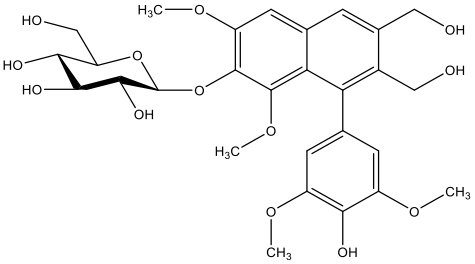

Chrysanthelignanoside D-

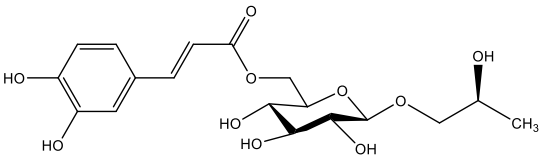

2S)-Propane-1,2-diol 1-O-(6-O-caffeoyl)-β-glucopyranoside

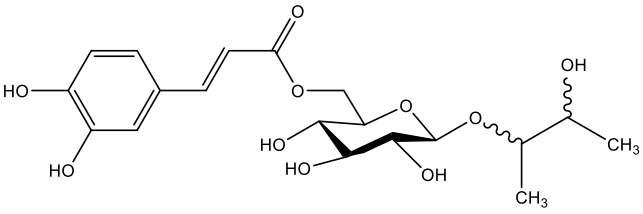

Butane-2,3-diol 2-O-(6-O-caffeoyl)-β-D-glucopyranoside

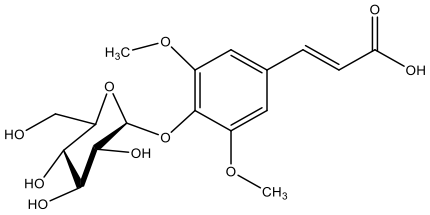

sinapoyl-4-O-ß-Dglucopyranoside

Myrica esculenta

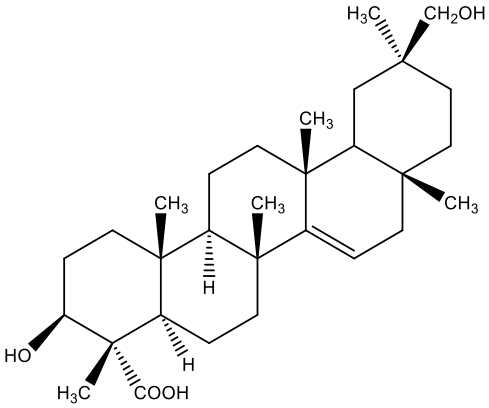

Dihydroxytaraxaranoic acid

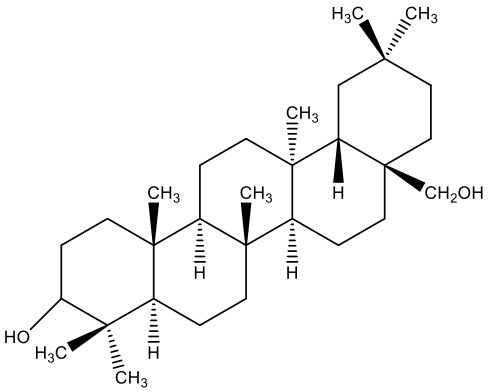

Dihydroxytaraxerane

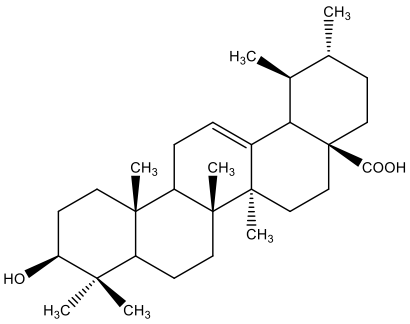

3-epi-ursonic acid

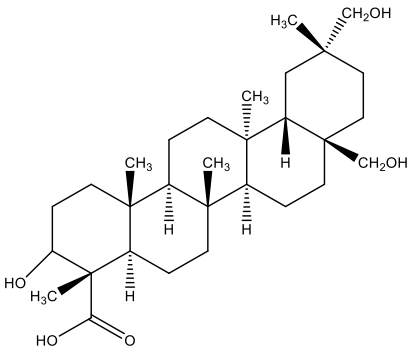

Trihydroxytaraxaranoic acid

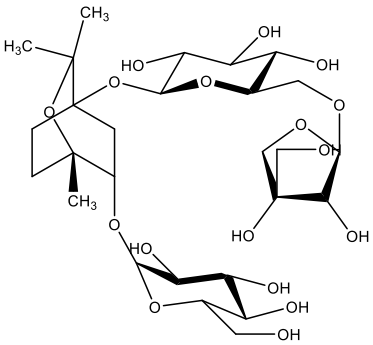

Myreculoside

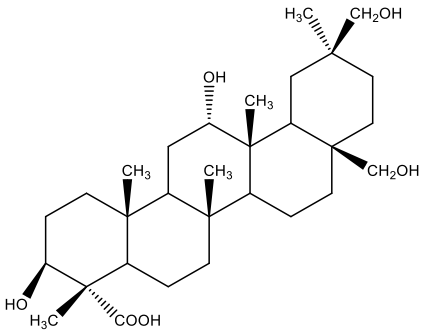

Tetrahydroxytaraxenoic acid

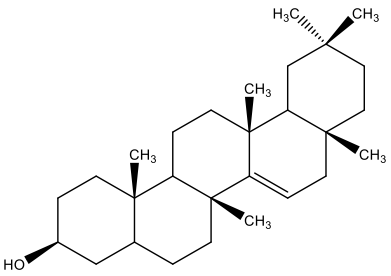

Taraxerol

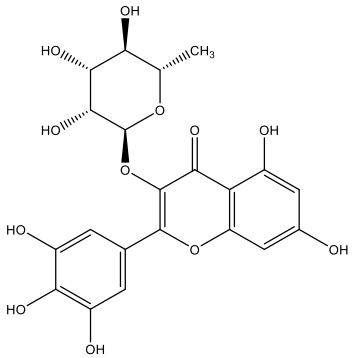

Myricitrin

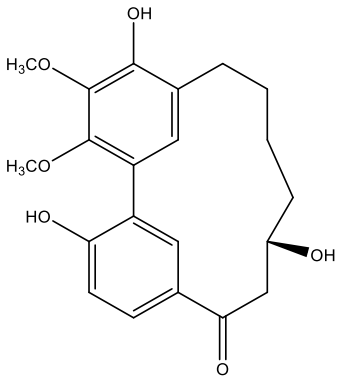

13-oxomyricanol

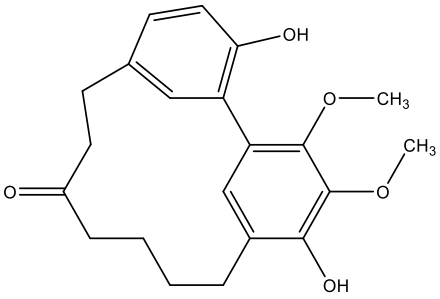

Myricanone

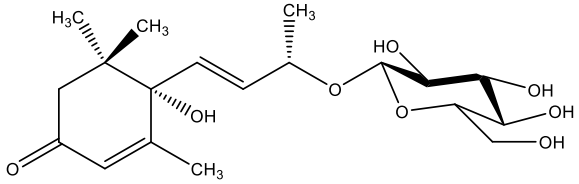

Corchoionoside C

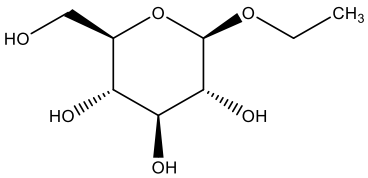

Ethyl-β-D-glucopyranoside

Hypericum uralum

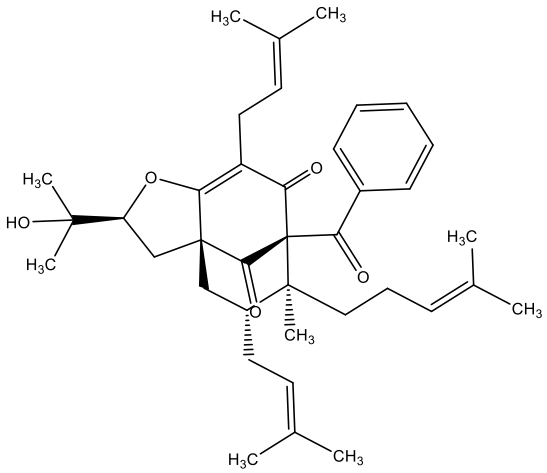

Uralione E

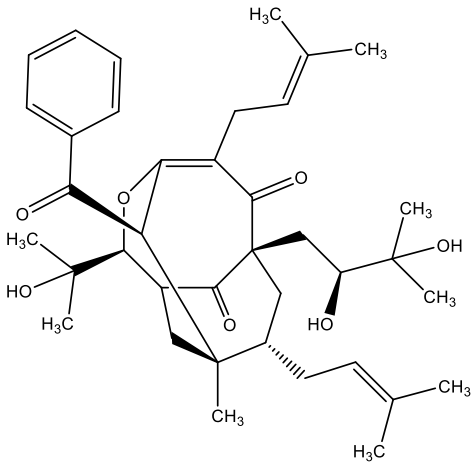

Uralione I

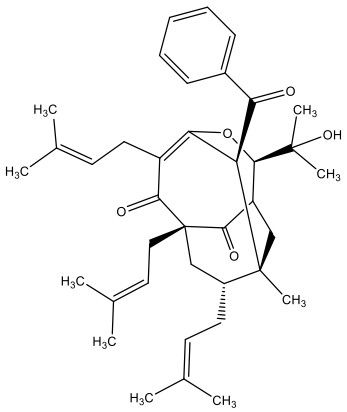

Uralione H

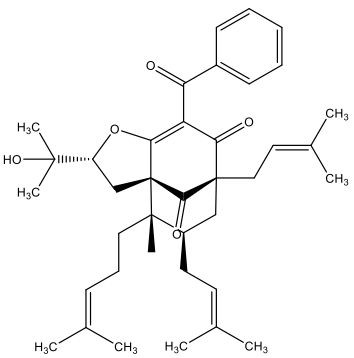

Uralione F

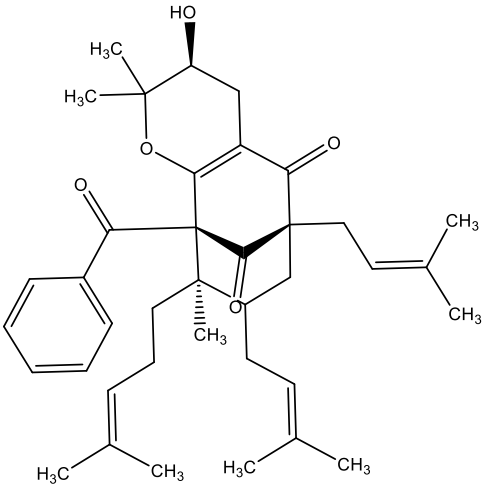

Uralione B

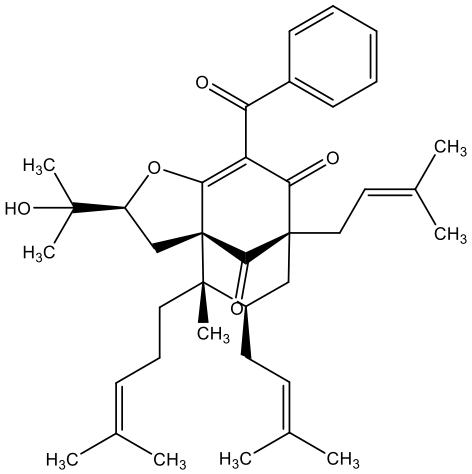

Uralione G

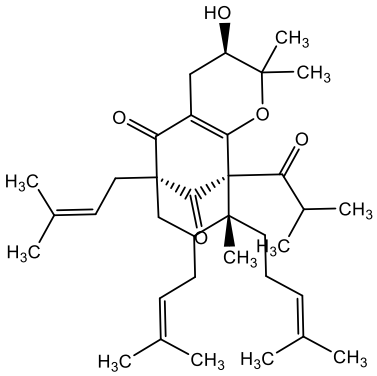

Uralione A

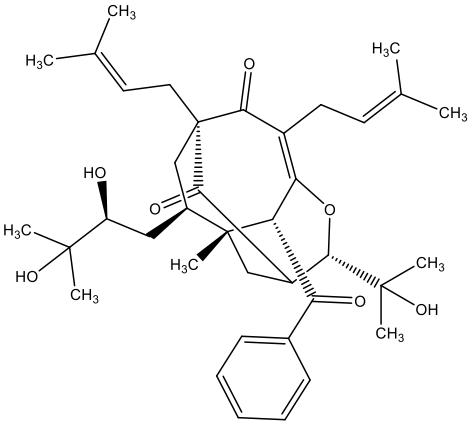

Uralione J

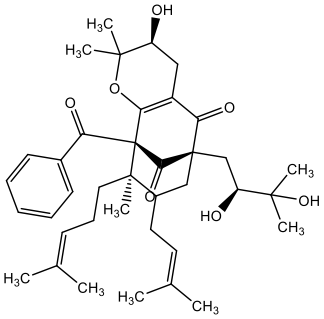

Uralione D

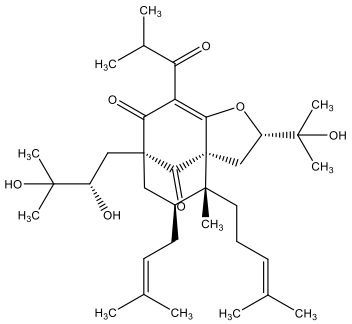

Uralione K

Persea americana

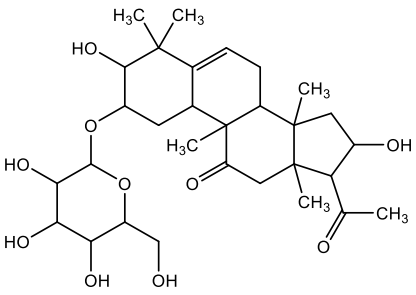

Perseapicroside A

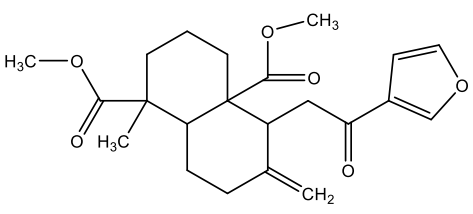

Dimethyl sciadinonate

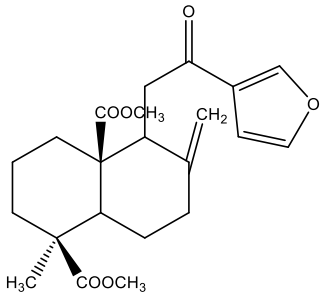

Dimethyl aciadinonate

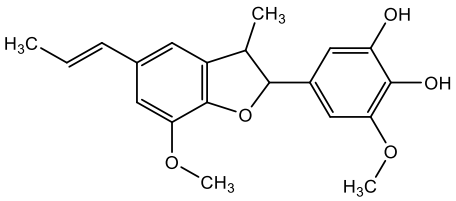

Obovatifol

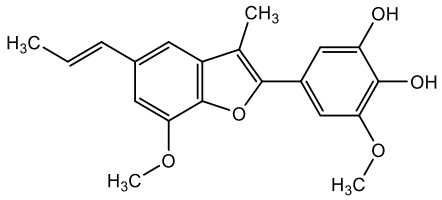

Obovaten

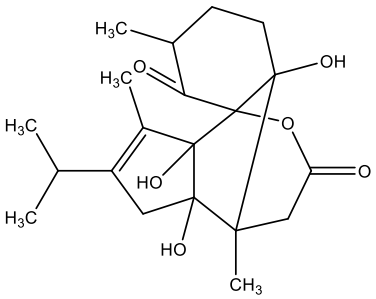

Anhydrocinnzeylanone

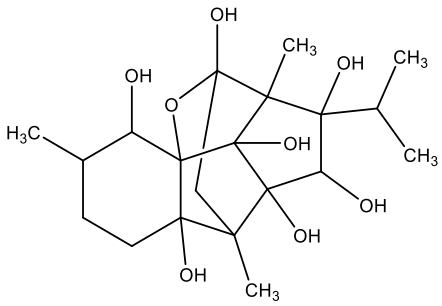

Ryanodol

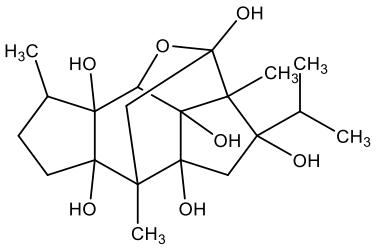

Perseanol

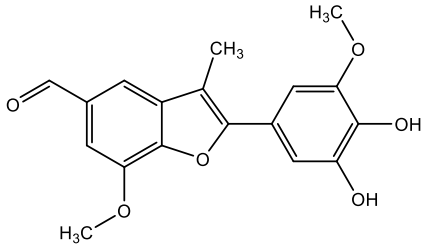

Perseal D

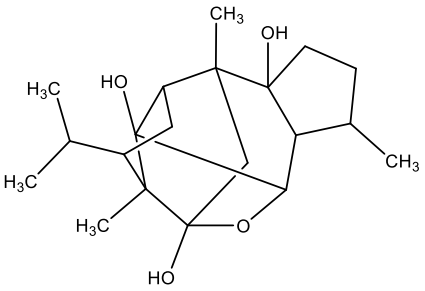

Indicol

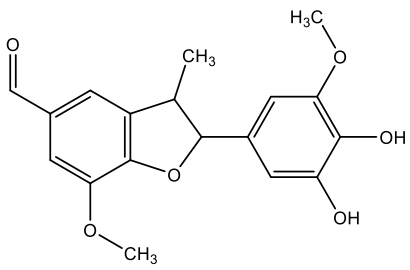

Perseal E

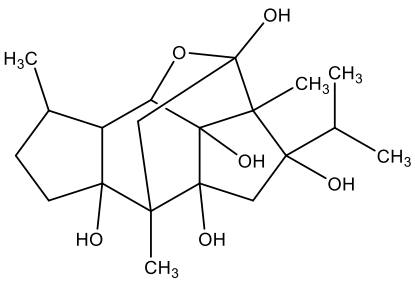

Vignaticol

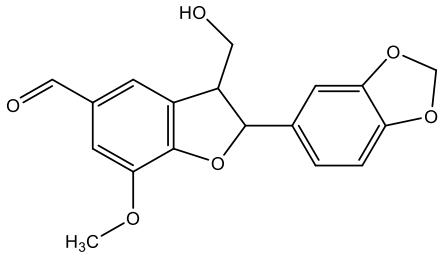

Perseal C

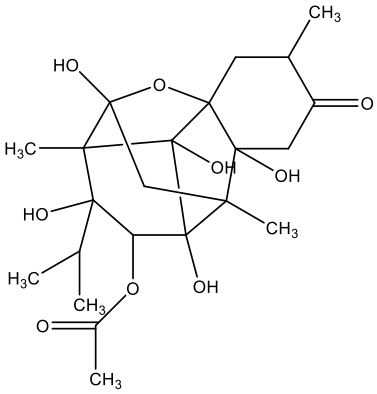

Garajonone

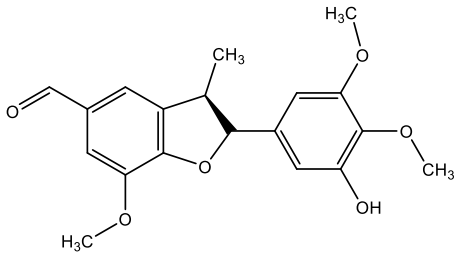

Obovatinal

Ageratina adenophora

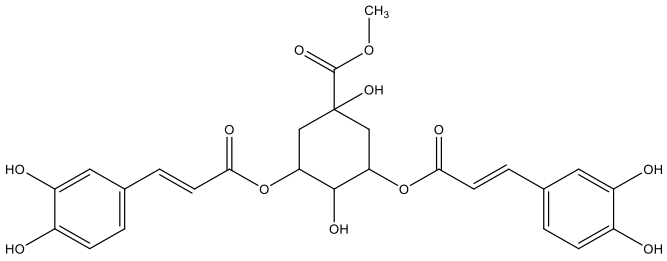

Macranthoin G

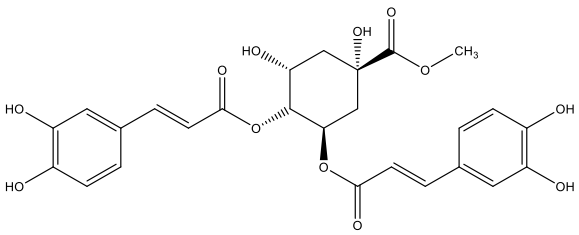

Macranthoin F

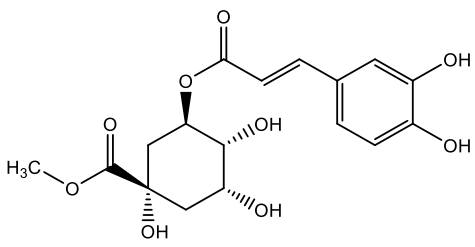

chlorogenic acid methyl ester

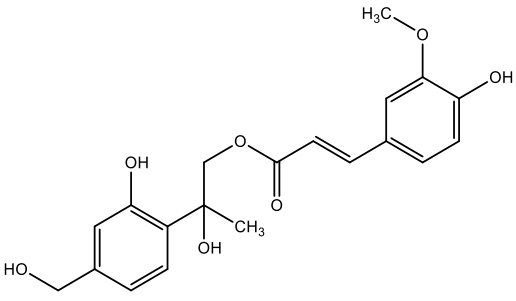

7-hydroxy-8,9-dihydrothymol-9-O-trans-ferulate

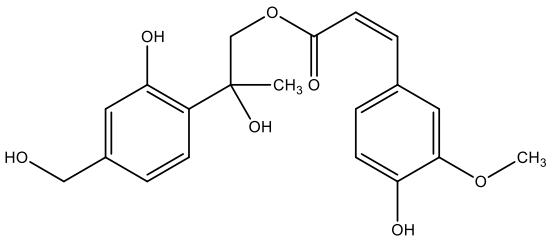

7,8-dihydroxythymol-9-O-trans-ferulate

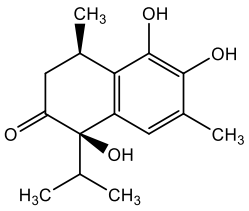

1,6-dihydroxy-1-isopropyl-4,7-dimethyl-3,4dihydronaphthalen-2(1H)-one

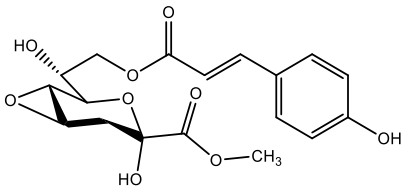

methyl (7R)-3-deoxy-4,5-epoxy-D-manno-2-octulosonate-8-O-trans-p-coumarate

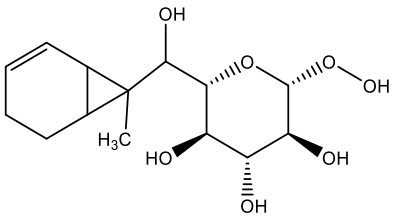

8-hydroxy-8-b-glucosyl-2-carene

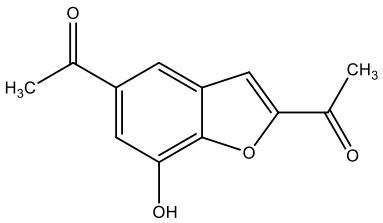

10-oxo-7-hydroxynordehydrotremetone

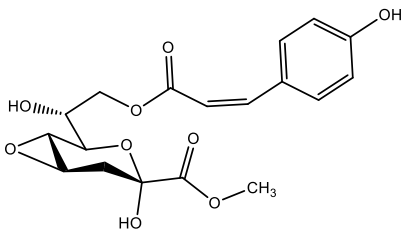

methyl (7R)-3-deoxy-4,5-epoxy-D-manno-2-octulosonate-8-O-cis-p-coumarate

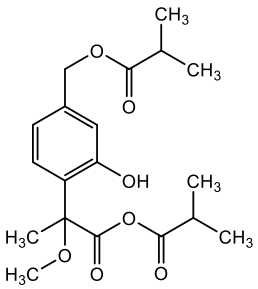

7,9-di-isobutyryloxy-8-methoxythymol

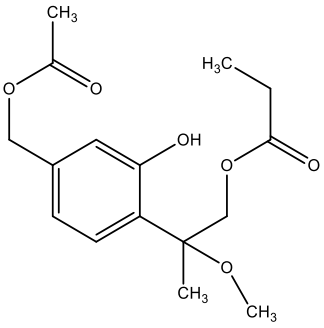

7-Hydroxycadinan-3-ene-2-one

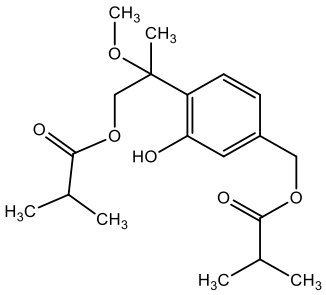

7-acetoxy-8-methoxy-9-isobutyryloxythymol

Cinnamomum ganduiflerum

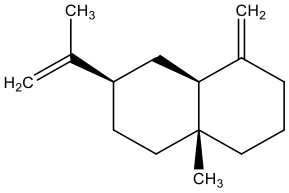

β-selinene

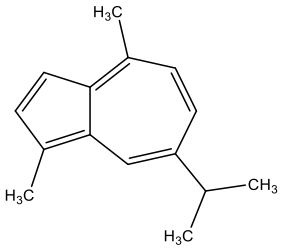

Guaiazulene

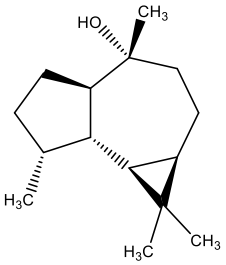

Globulol

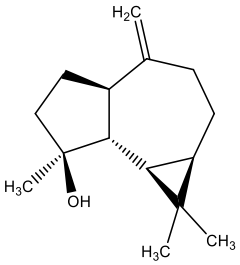

Spathulenol

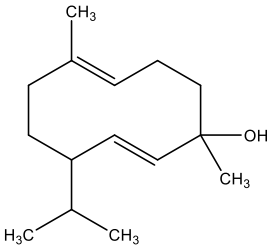

Germacrene D-4-ol

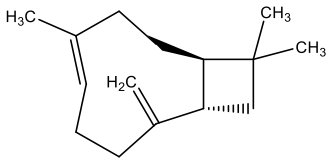

trans-Caryophyllene

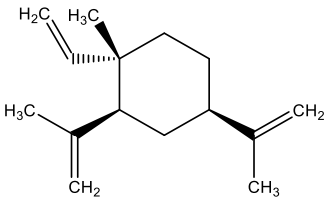

β-Elemene

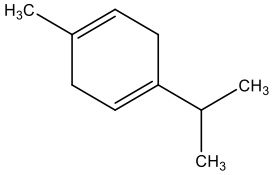

Gamma Terpinene

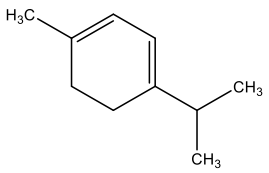

α-Terpinene

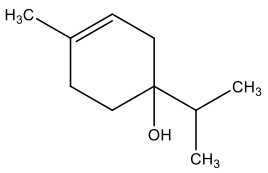

Terpinene-4-ol

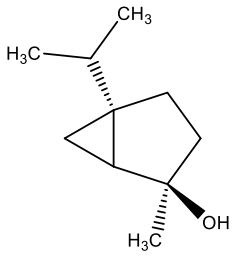

trans-Sabinene hydrate

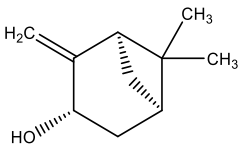

trans-pinocarveol

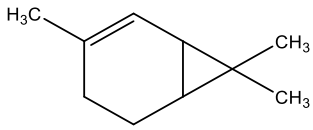

2-Carene

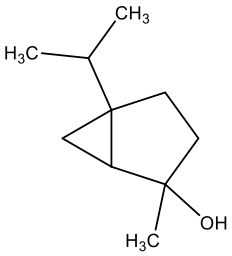

Cis-Sabinene hydrate

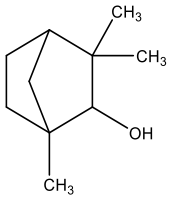

Fenchol

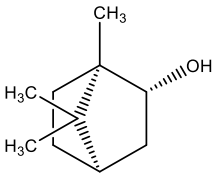

Isoborneol

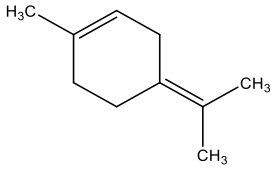

Terpinolene

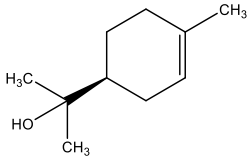

α-Terpineol

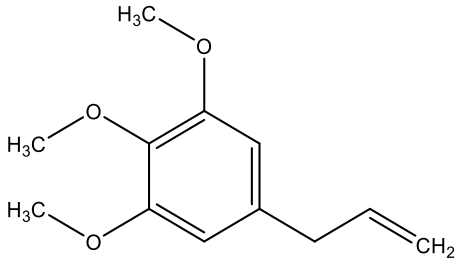

Elemicin

Figure S1. Structure of the selected 122 ligands.

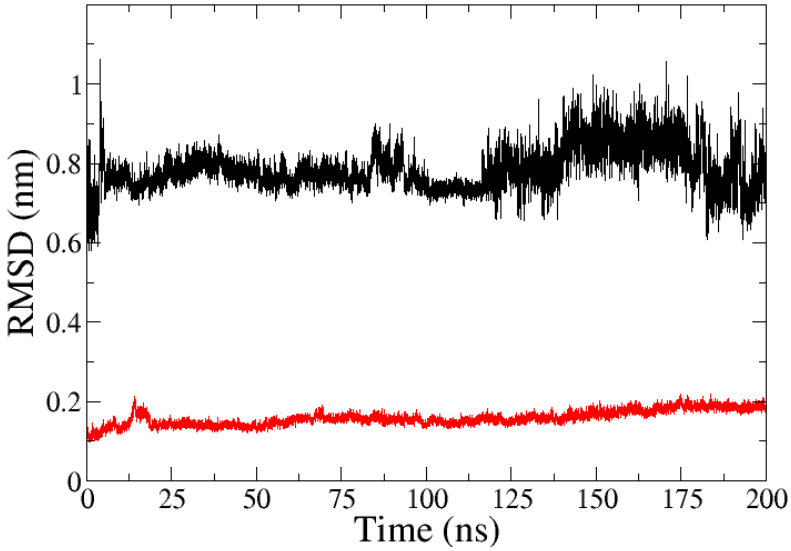

Figure S2. RMSD curve of myricetin (black) with respect to protein backbone (red).

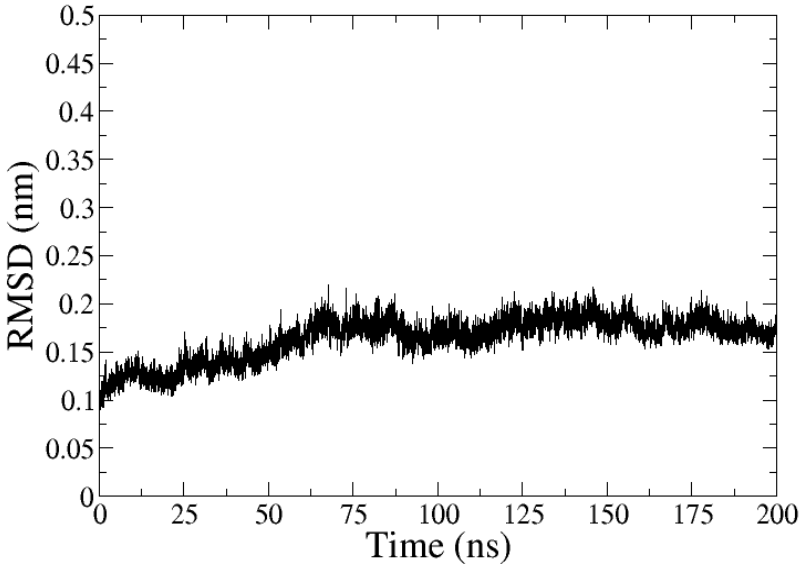

Figure S3. RMSD curve protein with respect to the protein backbone of the apostructure of 4GQR.

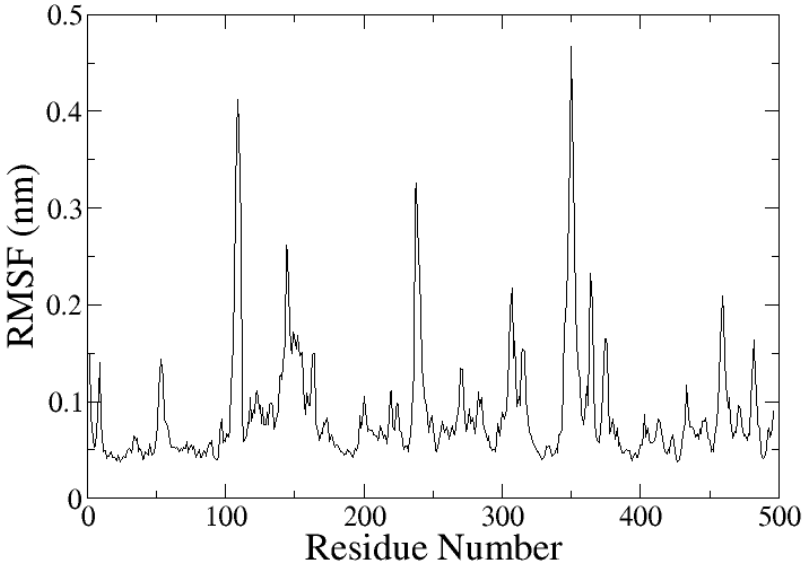

Figure S4. RMSF of α-carbon of the apostructure of 4GQR.

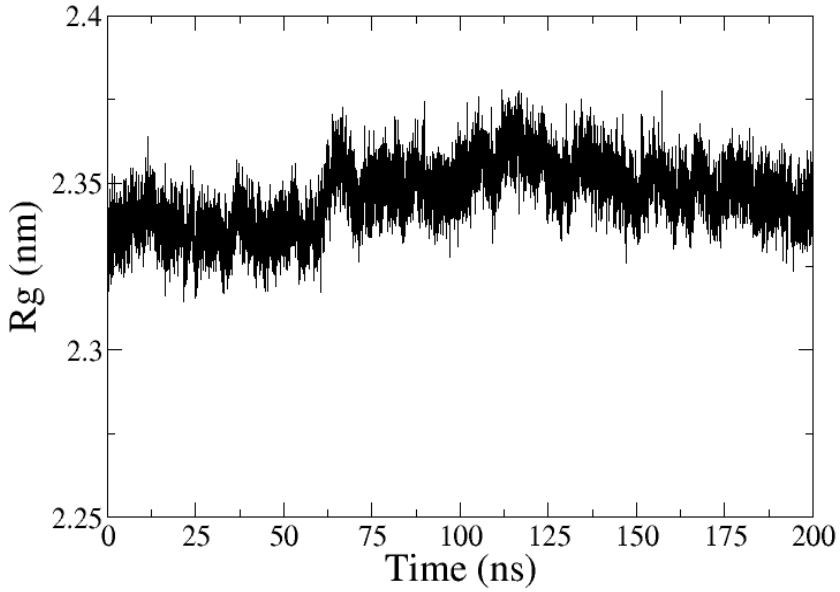

Figure S5. R_g of the apostructure of 4GQR.

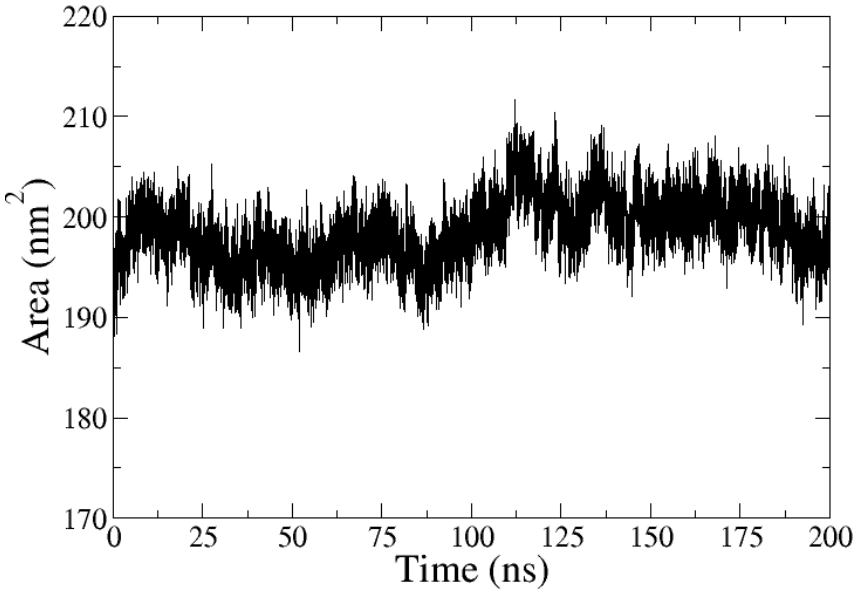

Figure S6. SASA of the apostructure of 4GQR.

Table S1. TPC of methanolic extracts of plant samples.

S.N.	Plant samples	TPC (mg GAE/g)
1.	*Psidium guajava*	24.29 ± 0.07
2.	*Myrica esculenta*	24.25 ± 0.03
3.	*Cinnamomum glanduliferum*	17.27 ± 0.02
4.	*Hypericum uralum*	16.86 ± 0.05
5.	*Chrysanthemum indicum*	9.70 ± 0.02
6.	*Picorrhiza kurrooa*	9.23 ± 0.02
7.	*Bunium bulbocastanum*	8.43 ± 0.26
8.	*Lawsonia inermis*	7.76 ± 0.01
9.	*Ageratina adenophora*	6.04 ± 0.01
10.	*Boerhavia sp.*	5.85 ± 0.01
11.	*Morus australis*	5.72 ± 0.01
12.	*Eclipta prostrate*	4.24 ± 0.07
13.	*Urtica ardens*	3.06 ± 0.01
14.	*Persea americana*	1.55 ± 0.04

15.	*Piper cubeba*	0.42 ± 0.01
16.	*Prunus persica*	0.41 ± 0.05

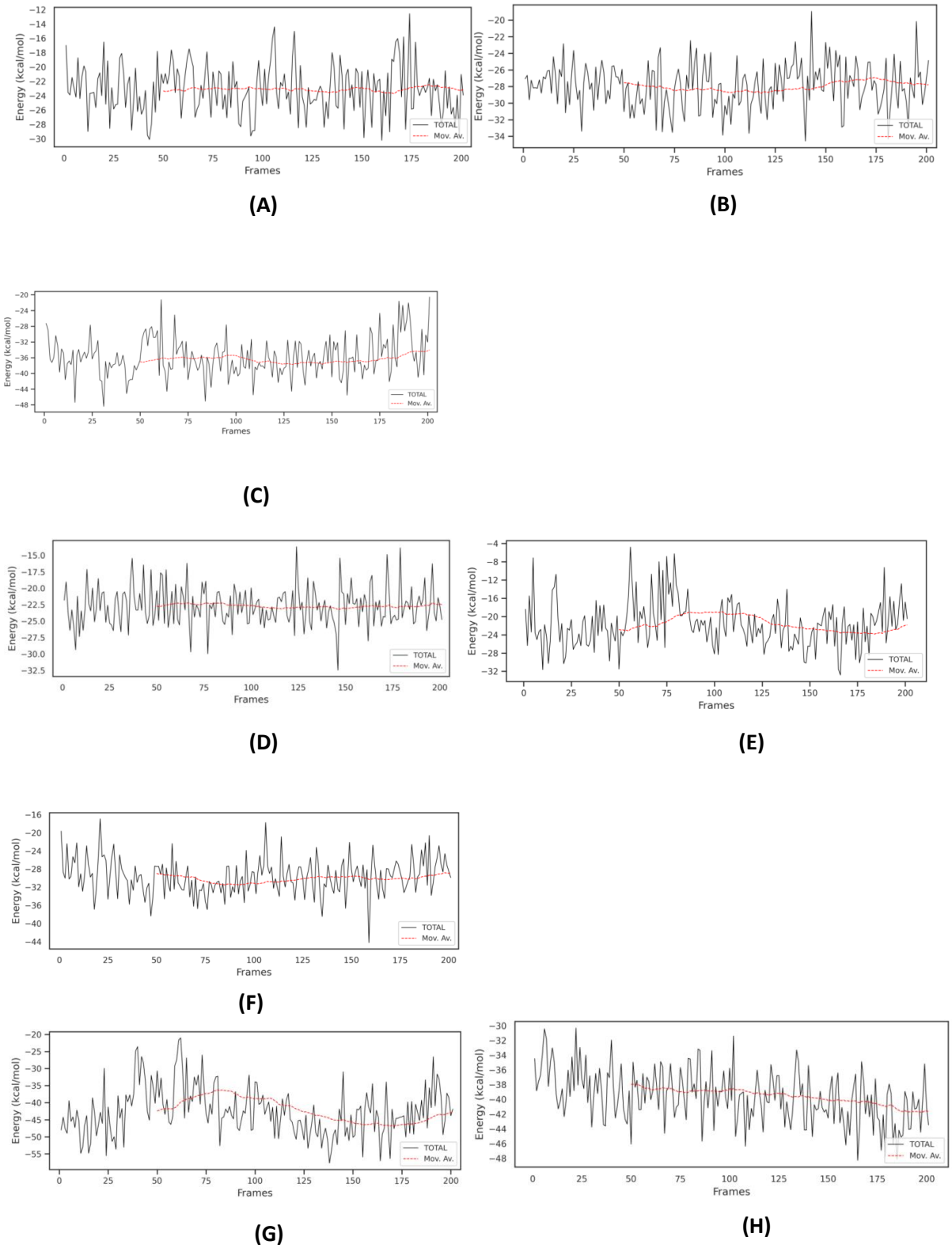

Figure S7. Binding free energy changes per frame of the last 20 ns (200 frames) of (A) Luteolin-3-glucoside complex, (B) Lawnermis acid complex, (C) Apigenin-7-O-rutinoside complex, (D) Dihydroxytaraxerane complex, (E) 3-epi-ursonic acid complex, (F) Perseapicroside A complex, (G) Macranthoin G complex, and (H) Macranthoin F complex

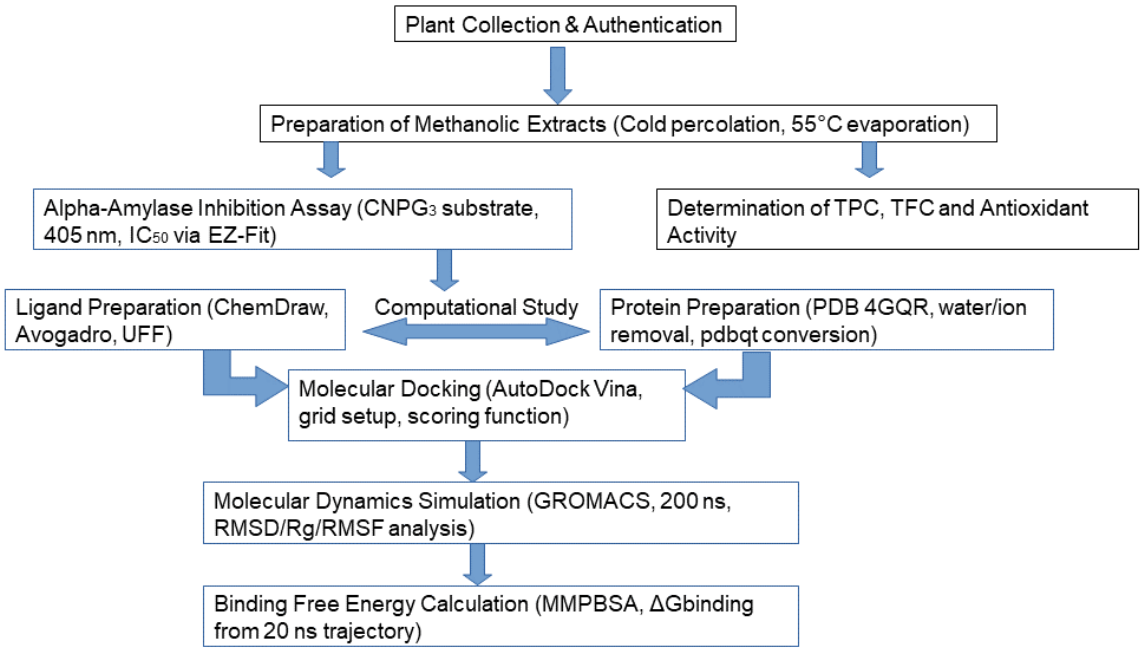

Figure S8. Integrated workflow outlining the experimental procedures and computational approaches employed.

Table S2. TFC of methanolic extracts of plant samples.

S.N.	Plant samples	TFC (mg QE/gm)
1.	*Hypericum uralum*	18.16 ± 0.05
2.	*Myrica esculenta*	10.31 ± 0.04
3.	*Chrysanthemum indicum*	10.04 ± 0.01
4.	*Boerhavia spp.*	8.79 ± 0.00
5.	*Ageratina adenophora*	8.25 ± 0.03
6.	*Lawsonia inermis*	7.22 ± 0.06
7.	*Morus australis*	5.03 ± 0.00
8.	*Cinnamomum glanduliferum*	4.53 ± 0.06
9.	*Eclipta prostrate*	2.92 ± 0.04
10.	*Bunium bulbocastanum*	2.29 ± 0.00
11.	*Persea americana*	1.94 ± .00
12.	*Urtica ardens*	1.67 ± 0.02
13.	*Picorrhiza kurrooa*	1.65 ± 0.01
14.	*Psidium guajava*	1.57 ± 0.00
15.	*Piper cubeba*	1.56 ± 0.01
16.	*Prunus persica*	1.24 ± 0.00

Table S3. Antioxidant activity in selected plants.

S.N.	Plant extracts (500 µg/mL)	DPPH radical scavenging activity in (%)
1.	Quercetin (standard)	98.34
2.	*Hypericum uralum*	40.81
3.	*Chrysanthemum indicum*	39.5
4.	*Myrica esculenta*	35.79
5.	*Ageratina adenophora*	25.5
6.	*Lawsonia inermis*	23.5
7.	*Cinnamomum glanduliferum*	21.48
8.	*Persea americana*	17